Cyclic Behavior of Four-Limbed Circular CFST Latticed Beam-Columns

You-Fu Yang[1], Feng Fu[2] F.ASCE and Min Liu[1,3]

Abstract: Experimental tests to investigate the behavior of four-limbed circular concrete-filled steel tube (CFST) latticed beam-columns under constant axial compression and cyclic lateral force were carried out. Attention was paid to the effect of diameter-to-thickness ratio of limb tube D/T (51.5 and 24.9), axial compression level n (from 0.05 to 0.5) and type of limb (circular CFST and steel circular hollow section (CHS)) on the overall behavior, failure modes and load versus deformation relationship of the specimens. Additionally, the cyclic deterioration of stiffness, ductility and accumulated energy dissipation of the specimens were assessed for seismic design. According to this experimental study, it is found that, due to the interaction between limb tube and its concrete core, the seismic resistance of composite specimens is better than that of steel counterparts. Moreover, the seismic resistance of composite specimens generally reduces with the increase of D/T and n. A finite element (FE) model is further established to replicate the behavior of the specimens, and the simulated cyclic behavior of four-limbed circular CFST latticed beam-columns subjected to constant axial compression and cyclic lateral force agree well with experimental results. Parametric study on the lateral force versus displacement hysteretic curve of four-limbed circular CFST latticed beam-columns was performed using the verified FE model. Finally, an accurate restoring force model (RFM) to predict the lateral force versus displacement relationship of four-limbed circular CFST latticed beam-columns is developed, and the predictions are in good agreement with the numerical and experimental results.

Keywords: Four-limbed circular CFST latticed beam-columns; Cyclic lateral force; Experimental behavior; Finite element simulation; Restoring force model; Metal and composite structures.

[1]Professor, State Key Laboratory of Coastal and Offshore Engineering, Dalian University of Technology, Dalian 116024, China (corresponding author). E-mail: youfuyang@163.com

[2]Senior Lecturer, School of Science & Technology, City, University of London, EC1V 0HB, United Kingdom. E-mail: Feng.Fu.1@city.ac.uk

[3]Lecturer, School of Civil Engineering, Liaoning Technical University, Fuxin 125105, China. E-mail: minliu19930723@163.com

Introduction

Concrete-filled steel tube (CFST) is a composite member formed by filling concrete into thin-walled steel tube, and due to the enhancement of tube wall stability by the filled concrete and the confinement from the outer steel tube on the brittle concrete core, the CFST has the advantages of high strength, good plasticity, superior fatigue/impact resistance, fast-track construction process, and so on (Han et al. 2014; Lin et al. 2021). Recently, the CFST has been widely used in high-rise, long-span, heavy-load bearing, and anti-seismic composite structures (Han et al. 2014; 2020).

In practical engineering, when the slenderness ratio or load eccentricity of a structural member are large, the advantage of good compression performance of single CFST member is difficult to be displayed, and the strength of materials is also not effectively utilized. Under such circumstances, the latticed members consisting of several CFST limbs and the connecting lacings become a better choice to overcome the above-mentioned disadvantages of the single CFST (Matsui and Kawano 1988). The CFST latticed member generally refers to the structural member with the CFST as the limbs and hollow steel tube as the lacings, and the centroid axis of the lacings is in the same plane as that of the two limbs welded with them. According to the difference in the number of the limbs, two-, three- and four-limbed cross-sections are the common form of the CFST latticed members (Yang et al. 2018b). Overall, in comparison with single CFST member having identical load-carrying capacity, the CFST latticed member not only has similar properties, but also possesses lighter weight, greater flexural stiffness and better stability (DBJ/T13-51 2010). The CFST latticed members have been used in practice as beams, columns, piers or arch ribs (Kawano and Sakino 2003; Yang et al. 2018b), and in the future also have good application prospect in large complex engineering both on land and at sea.

During large seismic overloads, the capacity, stiffness, ductility and energy dissipation of the CFST latticed members are dominated by the structural behavior of CFST limbs and tube lacings, as well as the synergistic effect between CFST limbs and tube lacings. Therefore, since the CFST latticed members were first developed, many researchers have paid attention to their seismic behavior by conducting cyclic tests and numerical simulation (Yang et al. 2018b), and the research by Kawano et al. (1996) is one of earlier attempts to explore the elasto-plastic behavior and deformability of two-limbed circular CFST latticed beam-columns experimentally and theoretically. Table 1 summarizes the available cyclic tests on the CFST latticed beam-columns, in which L is the length of specimens, D and T are the diameter/width and wall thickness of steel circular/square hollow section (CHS/SHS) in the limbs respectively, d and t are the diameter and wall thickness of steel CHS lacings respectively, $f_{y,li}$ is the yield strength of limb tube, f_c' is the cylindrical compressive strength of concrete in the limbs, and n is the axial compression level. It can be seen that, the limbs of most specimens are circular CFST, and the n values are relatively small and have limited variation. Simultaneously, the experimental results show that, the seismic behavior of composite latticed specimens is better than that of steel counterparts; however, further cyclic tests of CFST latticed beam-columns are needed to fully understand the influence of key parameters on their seismic behavior. In addition to experimental studies, finite element (FE) modelling on the cyclic behavior of CFST latticed beam-columns were also carried out by the commercial software ABAQUS (Deng 2012; Huang et al. 2018; Yang et al. 2018b, 2019) and OpenSees (Huang 2015; Yuan et al. 2020). The results showed that, the cyclic behavior of three-limbed circular and four-limbed square CFST latticed beam-columns can be well predicted by the FE model in Yang et al. (2018b, 2019); however, due to the neglect of key influencing factors (e.g. fracture of steel tubes), the cyclic behavior of four-limbed circular CFST latticed beam-columns has not been accurately simulated by the available FE models. Moreover, the restoring force model (RFM) of CFST latticed beam-columns is the basis for nonlinear dynamic time-history analysis of composite structures. Currently, two RFMs for the four-limbed circular CFST latticed beam-columns (Luo 2013; Chen et al. 2014) have been proposed; however, the suitability of them is limited by incomplete tests and/or inadequate FE simulations.

Based on the above review and analysis, it is clear that comprehensive study on the cyclic performance of four-limbed circular CFST latticed members is still limited, which shows that further experiments and theoretical modelling are necessary to guide the engineering practice. In this study, the focus is on the cyclic behaviors of four-limbed circular CFST latticed beam-columns. The effect of D/T, n and type of limb on the performance of typical specimens under constant axial compression and cyclic lateral force was first investigated, and then a FE model aiming to well predict cyclic behavior of four-limbed circular CFST latticed beam-columns was developed. In addition, a new RFM was proposed on the basis of systematic parametric study, and the accuracy of the RFM was verified by the comparison with the numerical and experimental lateral force versus displacement hysteretic curves.

Experimental program

Information of the Specimens

The behavior of 1/5 scale four-limbed latticed columns in Tianjin International Convention & Exhibition Center or 1/10 scale four-limbed latticed piers in Ganhaizi Bridge (Huang 2015) was investigated experimentally while subjected to combined constant axial compression and cyclic lateral force. A total of eight four-limbed specimens with M-shape layout of the lacings, consisting of six specimens with circular CFST limbs and two specimens with steel CHS limbs as reference, were manufactured, and the lacings of all the specimens were the steel CHS. The design of composite specimens and steel specimens is in accordance to DBJ/T13-51 (2010) and GB50017 (2017), respectively, and takes into account laboratory site conditions, loading capacity of equipment, and limit of research funds. The length (L) of all the specimens was designed to be 1960 mm. The parameters varied in the tests included: 1) D/T, 51.5 and 24.9, which are less than the limit of circular CFST in relevant codes (ACI318-19 2019; ANSI/AISC360-16 2016; EN1994-1-1 2004; GB50936 2014); n, 0.05 (low compressive load), 0.25 (basic compressive load) and 0.50 (high compressive load); and type of limb, circular CFST and steel CHS, in which the values of D/T reflect the impact of material properties and geometric sizes, while the values of n reflect the influence of load level.

The axial compression level (n) of the specimens is expressed as:

$$n = \frac{N_0}{\varphi \cdot N_s} \qquad (1)$$

where, φ is the stability factor, N_0 is the constant axial compressive load, and N_s is the sum of the sectional strength of all the limbs, for the specimens with steel CHS limbs, $N_s = \sum_{i=1}^{4} f_{y,li,i} \cdot A_{s,i}$, and for the specimens with circular CFST limbs (Yang et al. 2022), $N_s = k_u \cdot (1.14 + 1.02\xi) \cdot f_{ck} \cdot \sum_{i=1}^{4} A_{sc,i}$, in which $A_{s,i}$ and $A_{sc,i}$ are the cross-sectional area of the ith steel CHS limb and circular CFST limb respectively, k_u is the coefficient related to f_c', when $f_c' \leq$40 MPa, k_u=1.1, and when f_c' >40 MPa, k_u=1.0, ξ is the confinement factor of circular CFST (Han et al. 2014), and f_{ck} is the characteristic compressive strength of concrete.

For the steel specimens, the stability factor (φ) related to the equivalent slenderness ratio (λ_e) is determined using GB 50017 (2017), while for the composite specimens, φ is calculated by:

$$\varphi = \frac{1}{2\bar{\lambda}_{sc}^2}\left(k_l - \sqrt{k_l^2 - 4\bar{\lambda}_{sc}^2}\right) \leq 1.0 \tag{2-1}$$

$$k_l = 0.81 + 0.56\bar{\lambda}_{sc} + \bar{\lambda}_{sc}^2 \tag{2-2}$$

$$\bar{\lambda}_{sc} = \frac{\lambda_e}{\pi}\sqrt{\frac{0.67 f_{y,li}}{(0.192 f_{y,li}/235 + 0.488)\cdot E_{s,li}}} \tag{2-3}$$

where, $\bar{\lambda}_{sc}$ is the nomolized slenderness ratio, and $E_{s,li}$ is the elastic modulus of steel. The equivalent slenderness ratio (λ_e) including the effect of shear deformation of the lacings can be obtained by the formulae in Yang et al. (2019).

The configuration and dimensions of the specimens is shown in Fig. 1, where l_0 is the internode length of the limbs, and h_0 and s_0 are the cross-sectional width along major and minor axis, respectively. The information of the specimens is listed in Table 2, where $P_{u,e}$ is the tested lateral capacity, $K_{a,e}$ is the tested elastic stiffness, and I_d is the ductility index.

The limb tubes and lacings of all the specimens were respectively fabricated by the cold-formed and seamless steel CHS, and each specimen had two square steel plates with the sizes of 520 mm×520 mm×20 mm as the endplates. During the production of the specimens, eight four-limbed steel latticed specimens together with one endplate were first completed according to the designed sizes and welding process. The limbs and the lacings were welded together by the fillet welds, and the welding quality met the relevant codes. There was no eccentricity at the connection nodes of the limbs and the lacings. Fresh concrete was poured into the limbs of six steel specimens to form the composite specimens. In order to guarantee the cohesion of the steel and concrete interface, the end plane of the concrete infill was polished to be flush with the limb tube before welding another endplate. Moreover, four stiffeners spaced 90 degrees and arranged symmetrically were also welded to the end of each limb tube to avoid unexpected end damage.

The properties of steel CHS in the limbs and steel CHS lacing were respectively obtained by standard tensile and compressive coupons, and the average values of the measured results are listed in Table 3. The mix proportion of concrete in the limbs was: cement=420 kg/m^3, fly ash=130 kg/m^3, limestone gravel=832 kg/m^3, river sand=800 kg/m^3, tap water=189.5 kg/m^3, and water reducer=6.88 kg/m^3. The slump and spread of fresh concrete were 270 mm and 661 mm, respectively. The compressive strength of concrete was obtained by the test on cubes with side length of 150 mm, and the measured average result at 28 days and when conducting cyclic test of composite specimens were 55.2 MPa and 73.8 MPa, respectively. The elastic modulus of concrete was acquired by compressive tests on prisms with side lengths of 150 mm, 150 mm and 300 mm, and the measured average result was 3.47×10^4 N/mm^2.

Testing Set-up, Loading Histories and Instrumentation

The testing set-up is indicated in Fig. 2. The specimen was treated as a beam-column with one end fixed and the other end free under in-plane cyclic lateral force. A manually controlled hydraulic jack was used to apply the constant axial compressive load (N_0), and a closed-loop servo-controlled hydraulic actuator was employed to apply the cyclic lateral forces/displacements. In order to avoid the overturning effect and ensure the fixed boundary conditions, the bottom endplate of the specimen was connected with a 40 mm thick steel plate by twenty high-strength bolts, whilst the steel plate was fastened to the ground by two rigid beams and four anchor bolts. The top endplate of the specimen was linked to a T-shaped connector with a web thickness of 30 mm by twenty high-strength bolts, and one roller was arranged between the flange of the T-shaped connector and the front end of the actuator to ensure free rotation of the top end of the specimen. The back end of horizontally placed actuator was fixed on the reaction wall, and the front end was connected with the flange of the T-shaped connector by four high-strength bolts. The front end of vertically placed hydraulic jack was acted on a load cell, and another roller through cross-sectional centroid was placed between the load cell and the top of the specimen. The back end of vertically placed hydraulic jack together with a roller system along the loading direction were fixed on a rigid reaction frame, to ensure that the hydraulic jack moved freely with the lateral movement of the specimen.

The sequence history of force and displacement, which requires pre-determination of the yield force/displacement of the specimen, was widely used in the cyclic tests of single CFST beam-columns (Varma et al. 2004). However, the applicability of this method to cyclic tests of four-limbed circular CFST latticed beam-columns is unclear, and unsuitable loading regime may lead to premature failure or non-failure of the specimens. Therefore, in order to ensure the stable loading and obtain reliable test results, the displacement-controlled loading protocol was adopted in the present study according to existing guidelines and studies (ATC-24 1992; Yang 2018b, 2019). The history of lateral displacement at the top of the specimen corresponding to the *i*th loading step (δ_i) is shown in Fig. 3, where N_c is the number of cycles, which are determined with reference to the recommendations in ATC 24 (1992), and δ_0 is the nominal yield displacement, which is set to be identical for easy comparison, i.e. δ_0=10 mm. During the tests, the loading rate was controlled by the frequency of running a complete cycle, that is, when $j \leq 2$, $2 < j \leq 6$, $j=7$, $j=8$, $j=9$ and $j \geq 10$, the loading frequencies were 0.01Hz, 0.008Hz, 0.006Hz, 0.004Hz, 0.003Hz and 0.002Hz, respectively.

The generalized displacements were measured by eight displacement transducers (DTs) attached at top endplate and one limb, and the localized strains were measured by five strain gauges pasted on outer wall of two limbs and one lacing, as demonstrated in Fig. 2. In addition, a rigid frame was specially fabricated to hold the displacement transducer in different spatial positions.

Overall Behavior and Failure Modes

The recording of the tests showed that, for all the specimens, there was no displacement of the bottom endplate, and the connection between the limbs and the endplate was not damaged, indicating that no overturning effect occurred and the fixed boundary conditions were achieved. The failure process of all the specimens was dominated by the damage of the limb tubes, the limb-lacing KT-joints and/or the lacings. Generally, with the increase of δ_i, the local buckling with interval convexity and concavity first occurred near the root of the limbs of two steel specimens, and there were no further damage of lacings when D/T=51.5 or a few lacings with coupled global and local buckling when D/T=24.9 until the end of the tests. The outward local buckling of limb tube first happened to the root of most composite specimens, except that the cracking of limb tube in the limb-lacing KT-joint first happened to specimen C-B-0.05 and the local/global buckling of lacings happened to specimen C-B-0.25. When the lateral displacement increased to a certain extent, these three kinds of damage coexisted in the composite specimens, and further propagated with the increase of δ_i until the end of the tests. In addition, the good integrity of circular CFST latticed specimens during and after the tests showed that, the coupling behavior of four limbs could be ensured due to the presence of lacings, although the damage occurred to a number of lacings and KT-joints.

Fig. 4(a) shows the tested failure modes of the specimens, where the symbols ① through ⑤ respectively represent local buckling of limb tube, cracking of limb tube in the KT-joints, coupled global and local buckling of diagonal lacing, cracking/fracture of limb tube and fracture of diagonal lacing. For the steel specimens, the interval local buckling of CHS limbs mainly appears near the root, and further coupled global and local buckling of lacings occurs to the one with a smaller D/T. It should be noted that, the local buckling of limb L_1 in the specimen S-A-0.25 occurs at a location of (0.09~0.14)L away from the bottom endplate, which maybe due to the local out-of-arc deformation of the limb tube. However, under the same n value, the composite specimens have more complicated failure modes than steel counterparts, that is, additional cracking of limb tube in the KT-joints and coupled global and local buckling of lacings happen to specimen C-A-0.25, while coupled global and local buckling, even wall fracture, of more lacings occur to specimen C-B-0.25. The cracking of limb tube in the K-joints is mainly caused by the insufficient load-carrying capacity of tube wall under local complex stresses. In general, for the composite specimens, the number of positions with additional failure increases with the improvement of n, which mainly due to the more significant second-order effect under axial compression. Overall, the abovementioned failure modes of four-limbed circular CFST latticed specimens have also been observed in the previous experiments (Deng 2012; Huang et al. 2018; Chen et al. 2014; Huang 2015; Yuan et al. 2020).

Fig. 5 demonstrates the representative failure modes of concrete core in the CFST limbs. It can be observed that, the failure of concrete core is evidently related to that of limb tube, i.e., the localized compound crushing and cracking are formed at the local buckling position of limb tubes, and the tensile fracture appears at the cracking/fracture position of limb tubes. Simultaneously, the formation of indentation is caused due to the local compression of diagonal lacings near the KT-joints. It can also be seen from Fig. 5 that, there is no obvious wear track at the contact area between the limb tube and its concrete core, that is, no evident slippage occurs to their interface, which is similar to the findings in studies of Han et al. (2009) and Ji et al. (2014), meaning that the limb tube and its concrete core generally function cohesively as a unit.

Variation of Forces and Deformations

Based on the readings of DT_6 and DT_7 in Fig. 2, it was found that, the maximum relative torsion angle of the specimens (i.e. ratio of relative displacement to the distance) varied between 0.23% and 0.70%, indicating that the torsion of the specimens during the tests was limited, and its influence on the variation of forces (deformations) could be ignored.

The recorded lateral displacement along the length of typical specimens based on the readings of DT_0 through DT_5 in Fig. 2 is displayed in Fig. 6, where $\delta_{1,i}$ is the lateral displacement of the *i*th measuring point in the first cycle of each loading level, h_i is the distance between the *i*th measuring point and the bottom end, and p is the ratio of lateral force corresponding to $\delta_{1,i}$ to lateral capacity defined later, while a negative p value represents the stage after reaching the lateral capacity. It can be found that, generally, $\delta_{1,i}$ is distributed linearly along the length direction when $p \leq 0.6$ and basically symmetric in two loading directions. When p is between 0.6 and 1.0, the drift angle between two vertical measuring points increases gradually from bottom to top. In the post-peak stage, the distribution characteristic of $\delta_{1,i}$ is similar to that of structural frames with diagonal bracings, i.e. superposition of flexural deformation of four limbs and shear deformation of diagonal lacings.

Additionally, while p is the same, the CFST latticed specimen results in a larger $\delta_{1,i}$ than its steel counterpart, namely, a better deformability is achieved.

Fig. 7 shows the lateral force (P) versus drift angle (δ_t/L) hysteretic curve of the specimens, where δ_t is the lateral displacement at the top of the specimens. The recorded peak force in two loading directions of the $P-\delta_t/L$ curve is taken as the lateral capacity ($P_{u,e}$). It is indicated that, overall, the $P-\delta_t/L$ hysteretic curve of all the specimens is stable and no pinching characteristics is included. When n is consistent, the load-carrying capacity of steel specimens declines rapidly after reaching $P_{u,e}$ due to the serious local buckling of steel CHS limbs; however, due to the interaction between limb tube and its concrete core, the composite specimens have a wider $P-\delta_t/L$ hysteretic curve and a slower decrease in the load-carrying capacity after achieving $P_{u,e}$ than steel counterparts, exhibiting a better seismic resistance behavior. For the composite specimens, the higher the n value and the smaller the D/T value, the wider the $P-\delta_t/L$ hysteretic curve is. This can be explained that, within a certain range of n values (e.g. ≤ 0.5 in this study), the three-dimensional confinement to concrete core in the limb tube is better than the damage caused by the increase of n, which leads to a better structural property of circular CFST limbs, and the confinement effect of the tube in the CFST limbs on its concrete core increases with the decrease of D/T (Han et al. 2020).

The effect of parameters on $P-\delta_t/L$ backbone curve of the specimens is displayed in Fig. 8. It is shown that, the lateral force (P) in both loading directions generally experiences three stages, i.e., approximately linear increasing, nonlinear increasing and post-peak declining, as the drift angle (δ_t/L) increases. While n is kept constant, the composite specimens possess a higher elastic stiffness, a larger drift angle corresponding to $P_{u,e}$ and a slower decline rate of load-carrying capacity than the reference steel specimens. In addition, for the composite specimens, with the increase of n and the reduce of D/T, the elastic stiffness and drift angle corresponding to $P_{u,e}$ increase, while the decline rate of load-carrying capacity decreases at the post-peak stage.

Fig. 9 exhibits the effect of parameters on lateral force (P) versus strain (ε) hysteretic curves, where 'L' and 'T' in the brackets represent the longitudinal and transverse strain at the measuring points, respectively, and ε_y is the yielding strain of steel. It can be seen that, irrespective of the type of limb, the specimens with a smaller D/T generally possess a wider $P-\varepsilon$ hysteretic curve when n is the same, as the stability of steel CHS limb and the confinement of outer tube in the circular CFST limbs to its concrete core are enhanced. The strain development at point A is more sufficient than that at point B because of the difference in bending moments at the two points, while ε_L of the lowest diagonal lacings gradually develop into complete compression from symmetric coexistence of tension and compression due to the accumulated damage. In addition, after the tests completed, the maximum ε_L at points A and C is much larger than ε_y; however, the maximum ε_L at point B only approaches ε_y. It is shown in Fig. 9(a) that, the feature of $P-\varepsilon$ hysteretic curve at the same measuring point of composite specimen is generally similar to that of the reference steel specimen, whilst the former has a wider $P-\varepsilon$ hysteretic curve than the latter due to the improved performance of circular CFST limb than steel CHS limb. It is further shown in Fig. 9(b) that, for the composite specimens, the covered area in the second and fourth quadrants of $P-\varepsilon$ hysteretic curve increases with the increase of n. The $P-\varepsilon_L$ hysteretic curve is fusiform when n equals to 0.25 and 0.5; however, the $P-\varepsilon_L$ hysteretic curve is pinched in the later period when n=0.05, which may be caused by the cracking/fracture of limb tubes (see Fig. 4).

Mechanical Factors

Fig. 10(a) shows the influence of parameters on lateral capacity of the specimens, where $P_{u,e+}$ and $P_{u,e-}$ are the lateral capacity in 'push' and 'pull' directions, respectively, and their average values ($P_{u,e}$) are given in Table 2. It can be seen that, the lateral capacity of composite specimens is evidently higher than that of steel counterparts, considering that the load-carrying capacity of the limbs in the former is higher than that of the limbs in the latter due to the constraint effect of limb tube on its concrete core. On average, $P_{u,e}$ of composite specimen with D/T of 51.5 and 24.9 is 95.0% and 22.6% higher than that of its steel counterpart, respectively. While n is the same, the composite specimens with D/T of 24.9 result in a 18.0%-53.7% higher $P_{u,e}$ than those with D/T of 51.5, as the limb tube having a smaller D/T produces a stronger constraint to its concrete core (Han et al.

2014). For the composite specimens with D/T=24.9, $P_{u,e}$ decreases with the increase of n due to the impact of axial compression on the initial cumulative damage and the second-order effect, and $P_{u,e}$ of n=0.25 and n=0.50 is 5.0-9.6% and 14.6-18.3% lower than that of n=0.05, respectively. For the composite specimens with D/T=51.5, however, $P_{u,e}$ slightly increases with the increase of n. This may be due to the size deviation caused by the welding of thin-walled steel CHS, which reduces the lateral capacity of the specimens with a relatively small n.

The effect of parameters on elastic stiffness of the specimens measured by the initial slope of the $P-\delta_t$ curve is shown in Fig. 10(b), where $K_{a,e+}$ and $K_{a,e-}$ are the elastic stiffness in 'push' and 'pull' directions, respectively, and their average values ($K_{a,e}$) are also listed in Table 2. It is shown that, due to the interaction between limb tube and its concrete core, $K_{a,e}$ of composite specimen with D/T of 51.5 and 24.9 equals to 1.207 and 1.234 times that of the reference steel specimen, respectively. When n is the same, the composite specimens with D/T=24.9 lead to a 30.2~43.1% higher $K_{a,e}$ than those with D/T=51.5, considering that under the same tube diameter a smaller D/T causes a larger cross-sectional moment of inertia and a stronger constraint of limb tube to its concrete core. Furthermore, under the same D/T value, the elastic stiffness of composite specimens reduces when n increases due to the enhanced initial damage under a larger axial compression, and $K_{a,e}$ at n=0.25 and n=0.50 is 4.2~11.7% and 7.3~15.6% lower than that at n=0.05, respectively.

The ductility index (I_d) of the specimens in two loading directions can be computed by the following equation (Yang et al. 2019):

$$I_d = \frac{\delta_{t,0.85}}{\delta_{t,y}} \tag{3}$$

where, $\delta_{t,0.85}$ is the lateral displacement when $P = 0.85P_{u,e+}(P_{u,e-})$ in the post-peak phase of the $P-\delta_t$ backbone curve, and $\delta_{t,y}$ is the yield lateral displacement, which equals to $P_{\mathrm{u,e+}}/K_{\mathrm{a,e+}}$ or $P_{\mathrm{u,e-}}/K_{\mathrm{a,e-}}$.

The I_d value of all the specimens is taken as the average value of two loading directions; however, the I_d value of one loading direction is ignored, if the $P-\delta_t$ backbone curve has no descending stage or lateral force does not drop to $0.85P_{u,e+}(P_{u,e-})$. The obtained I_d of all the specimens is summarized in Table 2. The variation in the I_d value of the specimens is indicated in Fig. 10(c). As can be observed that, due to the combined action between limb tube and its concrete core, the I_d value of composite specimen with D/T of 51.5 and 24.9 is 69.9% and 34.9% higher than that of the reference steel specimen, respectively. In addition, the ductility of composite specimens show a decreasing trend with the increase of n and D/T, because of the existence of the second-order effect under axial compression and the reduction in confinement of concrete core from limb tube, and the I_d value at n=0.05 is 1.30~1.37 times and 1.37~1.47 times that at n=0.25 and n=0.50, respectively, while the I_d value when D/T=24.9 is 1.077-1.111 times that when D/T=51.5.

Deterioration of Stiffness

It is well known that, the stiffness of structural beam-columns decreases gradually while subjected to cyclic lateral force. Fig. 11 shows the deterioration of stiffness ($K_i/K_{a,e}$) of the specimens as N_c increases, where K_i is the secant stiffness under the *i*th loading cycle, and can be determined by the following equation (JGJ/T101 2015):

$$K_i = \frac{|+P_i|+|-P_i|}{|+\delta_{t,i}|+|-\delta_{t,i}|} \tag{4}$$

where, $+\delta_{t,i}$ and $-\delta_{t,i}$ are the peak lateral displacement in push and pull loading directions, respectively; and $+P_i$ and $-P_i$ are the lateral force relevant to $+\delta_{t,i}$ and $-\delta_{t,i}$, respectively.

It can be seen from Fig. 11 that, while $N_c \leq 6$, that is, the force reaches about half of lateral capacity, the deterioration of stiffness of composite specimens is slower than that of steel counterparts, mainly because the damage of concrete core is relatively slight during this stage, and the confinement of limb tube to its concrete core makes the performance of circular CFST limbs better than that of steel CHS limbs. While N_c is greater than 6, with the damage aggravation of concrete core under cyclic lateral force, the deterioration of stiffness of composite specimens is quicker than that of the relevant steel specimens. Moreover, when $N_c \leq 6$, the deterioration of stiffness of composite specimens with n of 0.50 is the quickest owing to the most severe initial damage of concrete core, and that of composite specimens with n of 0.05 and 0.25 has no consistent changing characteristics.

When N_c is larger than 6, generally, the composite specimens with n of 0.25 and 0.50 have a slower deterioration of stiffness than those with n of 0.05, considering that a higher axial compression results in a greater inhibition of tensile damage of concrete core due to the improvement in the bond between two materials and the compactness of concrete. At the same time, regardless of the type of limb, a quicker deterioration of stiffness is produced for the specimens with a larger D/T due to the reduced performance of the limbs.

Accumulated Energy Dissipation

The effect of parameters on the relationship between accumulated energy dissipation (E) and drift angle (δ_t/L) is displayed in Fig. 12. It can be observed that, compared with the reference steel specimens, the E value of composite specimens is significantly improved due to their higher lateral capacity, stiffness and ductility. Additionally, under the same conditions, the E value of composite specimens increases with the decrease of D/T and the increase of n. This can be explained that, the smaller the D/T value, the stronger the constraint of limb tube to its concrete core is, meanwhile, the increase of axial compression improves the bond between limb tube and its concrete core and the compactness of concrete core.

Finite Element (FE) Modelling

Description of the FE Model

To accurately replicate the cyclic behavior of four-limbed circular CFST latticed beam-columns, a finite element (FE) model was developed using the software package ABAQUS (2014).

The limb tubes and lacings in the composite beam-columns were simulated by the metal plasticity model using the von Mises yield criterion and the associated flow rule, and the mixed hardening plasticity model containing isotropic hardening and nonlinear kinematic hardening was utilized to characterize their cyclic behavior. The isotropic hardening was described by the changing of yield surface, and the nonlinear kinematic hardening was expressed by the changing of the back stress vector (ABAQUS 2014; Yang et al. 2018a, 2018b). In this study, the parameters in the mixed hardening plasticity model of steel tube were determined based on the linear interpolation of calibration values in previous tests (Shi et al. 2011; Jia and Kuwamura 2014) and further debugging by the coincidence between the simulated and measured cyclic behavior of all available circular CFST latticed beam-column specimens, and the final results are presented in Table 4, where $\sigma|_0$, Q_∞ and b_s are the parameters in the isotropic hardening model, and $C_{kin,1(\sim 4)}$ and $\gamma_{1(\sim 4)}$ are the parameters in the nonlinear kinematic hardening model. In addition, the ductile damage model recommended in ABAQUS (2014) consisting of ductile damage initiation criterion and damage evolution based on effective plastic displacement was adopted here to simulate the progressive damage (fracture) of steel tube under cyclic loading, and the details was given in Yang et al. (2019). Table 5 presents the parameters for ductile damage initiation criterion of steel tube in the specimens, where K_p is the strengthening coefficient, m_s is the hardening index, and C_1 and C_2 are the equivalent plastic damage strain under pure shear and uniaxial tension, respectively. Simultaneously, the measured properties from the tests were used for the elastic parameters of limb tubes and bracings, whilst the elastic modulus (E_s) and Poisson's ratio (μ_s) were respectively taken as 2.06×10^5 MPa and 0.3 when no test results were available. Moreover, during the tests, the influence of the deformation of other components (e.g. two endplates, stiffeners and loading plate, etc.) was very limited, and to simplify the modelling they were treated as the elastic materials with E_s and μ_s of 1.0×10^{12} MPa and 0.001, respectively.

The concrete damaged plasticity (CDP) model in ABAQUS (2014) was selected to model the complicate cyclic behavior of concrete core in the limb tubes of circular CFST latticed beam-columns. The recommended formula in ACI 318-19 (2019) was used to obtain the elastic modulus of concrete (E_c), i.e. E_c=4730$\sqrt{f_c'}$, and the Poisson's ratio of concrete was set to be 0.2. The plasticity parameters of concrete were same as those in Yang et al. (2018b), which were proved to be a good choice for the FE modelling on cyclic behavior of three-limbed circular CFST latticed beam-columns, that is, dilation angle=30°, flow potential eccentricity=0.1, ratio of initial equibiaxial compressive yield stress to initial uniaxial compressive yield stress=1.16, ratio of the second stress invariant on the tensile meridian to that on the compressive meridian=2/3 and viscosity parameter=0.0005.

The relationship between tensile stress and cracking displacement proposed by Goto et al. (2010) was used as the tensile constitutive model for concrete core in the limb tubes. The FE simulation results in the literature (Deng 2012; Yang et al. 2018b) demonstrate that, the compressive constitutive model for the concrete in the steel tube proposed by Han et al. (2007) was capable of well modelling the properties of concrete core in the limb tubes of circular CFST latticed members under cyclic loading. In this study, the same model was used for the compressive stress (σ_c)-strain (ε_c) relationship of concrete core in the limb tubes, and the details are as follows:

$$\frac{\sigma_c}{f_c'} = \begin{cases} 2\,\varepsilon_c/\varepsilon_p - \left(\varepsilon_c/\varepsilon_p\right)^2 & (\varepsilon_c/\varepsilon_p \le 1.0) \\ \dfrac{\varepsilon_c/\varepsilon_p}{\beta_0 \cdot \left(\varepsilon_c/\varepsilon_p - 1\right)^2 + \varepsilon_c/\varepsilon_p} & (\varepsilon_c/\varepsilon_p > 1.0) \end{cases} \tag{5}$$

where, $\varepsilon_p = (1300 + 12.5 f_c' + 800\xi^{0.2}) \times 10^{-6}$, $\beta_0 = (2.36 \times 10^{-5})^{[0.25+(\xi-0.5)^7]} \cdot (f_c')^{0.5}/2 \ge 0.12$.

For the CDP model in ABAQUS (2014), the elastic stiffness of concrete is damaged (or weakened) when the unloading stiffness in the softening stage of stress-strain curve is lower than the initial value, and in general the damage factors are used to represent the elastic stiffness loss of concrete. In this study, the suggested formulas by Birtel and Mark (2006) and Goto et al. (2010) were respectively used to calculate the damage factor (d) of concrete under compression and tension:

$$d = \begin{cases} 1 - \dfrac{\sigma_c \cdot E_c^{-1}}{\varepsilon_c^{pl} \cdot (1/b_c - 1) + \sigma_c \cdot E_c^{-1}} & \text{(under compression)} \\ 1.24(k_t/f_c') \cdot u_t^{ck} \le 0.99 & \text{(under tension)} \end{cases} \tag{6}$$

where, ε_c^{pl} is the compressive plastic strain; b_c is the ratio of compressive plastic strain to inelastic strain, which equals to 0.7, k_t is the maximum negative stiffness in the tensile softening stage (Goto et al. 2010), and u_t^{ck} is the cracking displacement.

While subjected to cyclic load, the elastic stiffness of concrete can partially recover. By reference to the existing results (Yang et al. 2019) and further calibration by the available test results, the stiffness recovery coefficient under compression (w_c) and tension (w_t) were set to be 0.2 and 0, respectively, i.e. the stiffness of concrete partially recovers when the stress state changes from tension to compression, and the stiffness of concrete does not recover when the stress state changes from compression to tension.

The limb tubes and bracings were modelled by the four-node reduced integrating shell elements (S4R), and to meet the calculation accuracy nine Simpson integral points were set along thickness direction of the shell elements. The concrete core in the limbs and other components were modelled using eight-node reduced integral three-dimensional solid elements (C3D8R). The structured meshing was realized by cutting the composite beam-columns into several regions, and the ideal mesh density was determined by gradually refining the meshing until the deviation of the calculation results of two adjacent meshing was less than 5%. In addition, the meshing at the crack prone positions (i.e. root of the limbs and limb-lacing KT joints) of the specimens was refined to capture their fracture process. The meshing of a typical FE model of four-limbed circular CFST latticed beam-columns is demonstrated in Fig. 13.

Based on the aforementioned test results, the interface between limb tube and its concrete core was replicated using surface-to-surface contact with finite sliding, which is consistent with the properties of steel-concrete interface under cyclic shear in the tests of Liu et al. (2022). The 'hard contact' in normal direction and the 'Coulomb friction' in tangential directions, which have been successively used in the FE simulation of composite columns under cyclic loading (e.g. Goto et al. 2010; Ma et al. 2018; Yang et al. 2018b), were used in the modelling. After referring to the previous research (Deng 2012; Luo 2013; Huang et al. 2018; Yang et al. 2018b) and further verified by the new test results, the tangential friction coefficient between limb tube and its concrete core was taken as 0.6. A consistent mesh density was set at the interface between shell and solid elements to ensure that the elemental nodes of two materials in the same position were coincident. Moreover, on the basis of ensuring accuracy and efficiency, the welding connection between limb tube and bracings/endplates as well as the interface between concrete and endplates were all simplified as the 'Tie' constraints.

The boundary conditions with one end fixed and the other end free were considered in the FE model of four-limbed circular CFST latticed beam-columns under cyclic lateral force, as shown in Fig. 13. All degrees of freedom of bottom endplate were restricted by setting as 'ENCASTRE' to reproduce the fixed boundary conditions achieved in the tests. One reference point (RP1) was set on the centroid of top endplate, and simultaneously a continuous distribution coupling constraint was established between RP1 and the upper surface of top endplate to restrict the degrees of freedom of RP1 outside the X-Z plane (i.e. U_Y=UR_X=UR_Z=0), so as to duplicate the in-plane free boundary conditions. Another reference point (RP2) together with a continuous distributed coupling constraint was set on the side centroid of top endplate to realize the application of cyclic lateral forces/displacements. Two analysis steps were defined, that is, in the first step the constant axial compressive load (N_0) was applied to the RP1, and in the second step the cyclic lateral forces (P) or displacements (δ_t) were applied to the RP2. Furthermore, the geometric nonlinear effects were considered in both analysis steps.

Additionally, the influence of initial geometric defects on the cyclic behavior of four-limbed circular CFST latticed beam-columns was analyzed by using the FE model, and the first buckling eigenmode of limb tubes and lacings in the composite specimens was determined as the initial geometric defects of the corresponding circular CFST latticed beam-columns in the first analysis step, as typically demonstrated in Fig. 14. The comparison between the simulated and measured results shows that, the influence of the initial geometric defects on the FE simulation results is limited when the defect factors are equal to $0.1T$ and $0.01D$ (Lai et al. 2016). As is well known, the welding residual stress has influence on the behavior of steel members. However, the parameters or processes related to the welding were not available for the tested specimens. Therefore, under the premise of ensuring the calculation accuracy, the effect of welding residual stress on the cyclic behavior of four-limbed circular CFST latticed beam-columns was temporarily not considered in the FE simulation.

Validation of FE model

The predicted failure modes of four-limbed circular CFST latticed beam-column specimens and steel counterparts in this study are displayed in Fig. 4(b). The contrast between the predicted and tested results shows that, overall, the failure modes, fracture and deformation of the limbs and out-of-plane deformation of lacings obtained by the FE simulation agree well with the tested results. The FE model is further used to identify the failure modes of four-limbed circular CFST latticed beam-columns. It is found that, generally, there are two kinds of failure modes, namely compression-shear failure and compression-flexure failure, and the equivalent slenderness ratio (λ_e) is the determining factor. Fig. 15 demonstrates the effect of λ_e on the failure modes of typical four-limbed circular CFST latticed beam-columns. It can be seen that, with the increase of λ_e, the area with high stress in the limb tubes and lacings is concentrated towards the bottom of limb tubes and the peak value of the Mises stress also shows a decreasing tendency, indicating that the compression-shear failure gradually changes to the compression-flexure failure.

The predicted $P-\delta_t/L$ hysteretic curves, lateral displacement distribution, $P-\varepsilon$ hysteretic curves and deterioration of stiffness of four-limbed circular CFST latticed beam-column specimens are compared with the tested results in Figs. 7 and 16, 17, 18, and 19, respectively. In Figs. 19(c and d), to clearly show the comparison results, the curves with n=0.25 and n=0.50 are shifted to the right by $0.01\delta_t/L$ and $0.02\ \delta_t/L$, respectively. It is shown that, the predicted results generally accord well with the tested ones. The comparison of mechanical factors of four-limbed circular CFST latticed specimens between the predicted and tested results is shown in Fig. 20, where $P_{u,fe}$ and $K_{a,fe}$ are the predicted lateral capacity and elastic stiffness using the FE model, respectively, and μ and σ denote the mean value and the standard deviation, respectively. The results of statistical analysis exhibit that, in general, the predicted lateral capacity and elastic stiffness of four-limbed circular CFST latticed specimens agree well with the tested results.

The above comparison proves that, overall, the cyclic behavior of four-limbed circular CFST latticed beam-columns can be well predicted by the FE model established in this study.

Restoring Force Model (RFM)

The restoring force model (RFM) is an important basis for the elastic-plastic seismic response analysis of complex members/structures (Fukumoto and Morita 2023). The experimental results of this study show that, the deformation characteristics of a CFST latticed beam-column is superimposed by flexure-type and shear-type under the combined action of constant axial compression and cyclic lateral force, and as a result it is appropriate to use shear layer model to describe its RFM, namely the mathematical model between lateral force and the corresponding displacement.

Key Parameters

The effect of parameters on $P-\delta_t$ hysteretic/backbone curve of four-limbed circular CFST latticed beam-columns is analyzed using the verified FE model. The basic parameters are: D×T=100 mm×2.3 mm, d×t=34 mm×2.3 mm, h_0=s_0=l_0=400 mm, n=0.4, f_c'=50 MPa, $f_{y,li}$=355 MPa, yield strength of lacing ($f_{y,la}$) is 355 MPa, and nominal shear-span ratio λ_m(=L/h_0) is 3.0. The FE modelling results are demonstrated in Fig. 21, where the black lines denote the relevant backbone curves. It can be seen that, the trend of $P-\delta_t$ backbone curves and the unloading/reloading criterion of $P-\delta_t$ hysteretic curves are mainly determined by D/T, $f_{y,li}$, f_c', d/t, n and λ_m. Additionally, $f_{y,la}$ only has an effect on the peak force of $P-\delta_t$ backbone curve of members with a small λ_m.

Detailed RFM

By careful observation and analysis of a large number of FE simulated $P-\delta_t$ hysteretic curves, it is found that, the RFM of four-limbed circular CFST latticed beam-columns can be denoted by the segmented lines in Fig. 22, where the line O-A(A′)-B(B′)-C(C′) represents the backbone curve, and the lines 1-2-1′-2′-1 (before reaching lateral capacity) and 3-4-5-3′-4′-5′-3 (after reaching lateral capacity) represent the unloading/reloading paths.

The Y-coordinate at point B(B′) (P_m) on the backbone curve of the RFM, i.e. lateral capacity, is defined as the force that first satisfies the following conditions: 1) the maximum tensile (shear) strain of steel tube at the limbs' root reaches 0.01, and 2) the peak force of $P-\delta_t$ backbone curve. Based on the regression analysis of the FE simulation results, the formulae of P_m can be expressed as:

$$\frac{P_m}{1.17V_u}=\begin{cases}\left[0.35-0.43n^{1.9}+\frac{P_m\cdot L}{1.17M_u}\right]^{0.71} & (k_v\le 0.85)\\ \left[f(n)\cdot(1.94n\cdot\xi-1.13n+1)\right]^{-0.49} & (k_v>0.85)\end{cases} \tag{7-1}$$

$$V_u=\begin{cases}V_{u,li}+V_{u,la} & (\lambda_m<\lambda_{m0})\\ M_u/L & (\lambda_m\ge\lambda_{m0})\end{cases} \tag{7-2}$$

$$V_{u,li}=\frac{0.52}{-0.22+\lambda_m^{0.5}}\cdot(-0.06+0.39\alpha_s^{2.57})\cdot(-3.23+0.81\xi^{-0.66})\cdot N_s \tag{7-3}$$

$$V_{u,la}=\frac{0.66\sum_{i=1}^{2}f_{y,la}\cdot A_{s,la,i}\cdot\sin\theta}{L/l_0} \tag{7-4}$$

$$k_v = (V_{u,li} + V_{u,la})/(M_u/L) \tag{7-5}$$

$$M_u = (0.95 + 0.16\xi^{-0.9}) \cdot r_c \cdot f_{y,li} \cdot \sum_{i=1}^{2} 1.1A_{s,li,i} \tag{7-6}$$

$$f(n) = 4.54n^2 - 2.8n + 1 \tag{7-7}$$

where, k_v is the shear strength ratio, λ_{m0} is the critical shear-span ratio determining iteratively by k_v=1.0, $V_{u,li}$ and $V_{u,la}$ are the shear strength of limbs and lacings, respectively, α_s is the cross-sectional steel ratio of circular CFST limbs (Han et al. 2020), $A_{s,li,i}$ and $A_{s,la,i}$ are the area of the *i*th limb tube and lacing in the same cross-section, θ is the angle between diagonal lacing and limb, and r_c is the distance between the barycenter of composite section and the centroid of limbs under compression.

The Y-coordinate at point A(A′) (P_y) on the backbone curve of the RFM corresponding to the end of elasticity is equal to $0.7P_m$. The initial slope of the backbone curve of the RFM, namely the elastic stiffness (K_a), can be expressed as:

$$K_a = \eta_K \cdot 3\sum_{i=1}^{2}\left(E_s \cdot I_{s,i} + 0.6E_c \cdot I_{c,i}\right)/L^3 \tag{8-1}$$

$$\eta_K = \begin{cases} (0.32 - 0.06n) \cdot \alpha_s^{-0.13} \cdot (d/t)^{-0.33} \cdot \lambda_m^{1.13} & (\bar{\lambda}_{sc} \le 0.46) \\ (1.34 - 0.48n) \cdot \alpha_s^{-0.13} \cdot (d/t)^{-0.13} \cdot \lambda_m^{0.14} & (\bar{\lambda}_{sc} > 0.46) \end{cases} \tag{8-2}$$

where, $I_{s,i}$ and $I_{c,i}$ are the cross-sectional moment of inertia of limb tube and its concrete core in the *i*th limb about the centroid axis of composite section.

The X-coordinate at point B(B′) ($\delta_{t,m}$) on the backbone curve of the RFM can be determined by:

$$\delta_{t,m} = [(6 + 6n^2 - 11.28n + 2.34\xi^{0.54}) \cdot \lambda_m^{-0.69} + 0.06n \cdot \lambda_m] \cdot \frac{P_m}{K_a} \tag{9}$$

The formula for the stiffness at descending stage B(B′)-C(C′) (K_T) of the backbone curve of the RFM is as follows:

$$K_T = \frac{-0.006\lambda_m^{1.58} \cdot \xi^{0.64}}{1 + 2.54n^2 - 3.49n + 0.66\xi} \cdot K_a \tag{10}$$

The unloading/reloading criterion of the RFM is as follows: 1) when unloading from point 1(3) to point 2(4), the stiffness of linear unloading equals to K_r, and the Y-coordinate at point 2(4) is $\eta_D \cdot P_r$, where P_r is the force at unloading point; 2) linear unloading continues to point 1'(3'), where point 1'(3') is the symmetric point of point 1(3) with respect to the origin of coordinates, and the transition point 5 is on the backbone curve and its Y-coordinate equals to $\eta_E \cdot P_r$; and 3) reloading continues along path 1'-2'-1 or 3'-4'-5'-3 until the next unloading/reloading cycle begins. The regression formula for the related coefficients is as follows:

$$\frac{K_r}{K_a} = \left(\frac{\delta_{t,m}}{\delta_r}\right)^c \tag{11}$$

$$\eta_D = 0.62n - 0.57[\ln(6.66\alpha_s)]^2 + 0.28 \tag{12}$$

$$\eta_E = [0.017(\ln\alpha_s)^3 + 1.07] \cdot (\lambda_m^{0.12} - 0.14) \cdot [0.18\ln(n) + 1.17] \tag{13}$$

where, δ_r is the displacement at unloading point, and c is 0.6 and 0 when $\delta_{t,m}/\delta_r$<1.0 and $\delta_{t,m}/\delta_r$ ≥1.0, respectively.

The comparison of key parameters in the RFM of four-limbed circular CFST latticed beam-columns between the simplified and FE simulation results is shown in Fig. 23, where, the parameters with subscripts ‘s’ and ‘fe’ are simplified and simulated values, respectively. It can be observed that, generally, the simplified formulae based on regression analysis can well predict the key parameters in the RFM of four-limbed circular CFST latticed beam-columns. The typical comparison between the RFM and the FE/test $P-\delta_t$ hysteretic curves is demonstrated in Fig. 24. It can be seen that, overall, the proposed RFM is capable of well predicting the $P-\delta_t$ hysteretic curves of four-limbed circular CFST latticed beam-columns.

The scope of application of the RFM is: D/T=22.7-83.3, d/t=10-20, $f_{y,li}(f_{y,la})$=235 MPa-460 MPa, f_c'=25 MPa-65 MPa, h_0/l_0=0.67-2.0, h_0/s_0=1.0-2.0, λ_e ≤80 and $n \leq 0.6$.

Conclusions

Based on the tests and FE simulation on the cyclic behavior of four-limbed circular CFST latticed beam-columns, the following conclusions can be drawn:

(1) The test results of typical latticed specimens show that, while subjected to constant axial compression and cyclic lateral force, the coupling behavior of four CFST limbs can be ensured due to the linkage of lacings, and the overall failure modes of circular CFST latticed are manifested as cracking of limb tube in the KT-joints due to the insufficient load-carrying capacity of tube wall under local complex stresses, coupled global and local buckling of diagonal lacings and local buckling

and/or cracking of limb tubes. Additionally, the localized compound crushing and cracking occur to concrete core in the CFST limbs.

(2) Along the length of CFST latticed specimens, the distribution of lateral displacement is analogous to that of structural frames with diagonal bracings. When n is the same, the CFST latticed specimens have a wider $P-\delta_t(\varepsilon)$ hysteretic curve and a slower decline in load-carrying capacity after achieving $P_{u,e}$ than steel counterparts due to the improved performance of circular CFST limbs; while a wider $P-\delta_t(\varepsilon)$ hysteretic curve is produced for the CFST latticed specimens with a larger n and a smaller D/T.

(3) While n kept unaltered, the CFST latticed specimen with D/T=51.5 results in 95% greater $P_{u,e}$, 20.7% greater $K_{a,e}$ and 69.9% greater I_d than the relevant steel latticed specimen, and for the CFST latticed specimen with D/T=24.9, the above enhance percentages are 22.6%, 23.4% and 34.9%, respectively. Moreover, $P_{u,e}$, $K_{a,e}$ and I_d of CFST latticed specimens with D/T=24.9 are 18.0%-53.7%, 30.2%-43.1% and 7.7%-11.1% higher than those of composite specimens with D/T=51.5, respectively, and overall the CFST latticed specimens with a smaller n lead to a higher value of $P_{u,e}$, $K_{a,e}$ and I_d.

(4) A FE model, which reasonably contains mixed hardening and progressive damage of steel tube as well as damaged plasticity and partial stiffness recovery of concrete core, is established using the ABAQUS, and the FE-simulated cyclic behaviors of two- and four-limbed circular CFST latticed beam-column specimens generally conforms with the experimental observations. The FE simulation results further show that, for four-limbed circular CFST latticed beam-columns, there are two kinds of failure modes, namely compression-shear failure and compression-flexure failure.

(5) By the FE modelling, the impact of key parameters on the $P-\delta_t$ hysteretic/backbone curve and unloading/reloading paths is discovered, and the RFM for the four-limbed circular CFST latticed beam-columns is further established based on the regression analysis of the FE simulation results. Generally, the simplified $P-\delta_t$ hysteretic curves according to the RFM are in good agreement with the FE simulation and test results.

Data Availability Statement

Some or all data, models or code that supports the findings of this study are available from the corresponding author upon reasonable request.

Acknowledgements

The studies in this paper are financially supported by the National Natural Science Foundation of China (Projects 51678105). The financial support is gratefully acknowledged.

References

[1] ABAQUS. 2014. "*ABAQUS standard user's manual, version 6.14*." Dassault Systèmes Corp., Providence, RI, USA.

[2] ACI 318-19. 2019. "*Building code requirements for structural concrete and commentary*." American Concrete Institute, Farmington Hills, MI.

[3] ANSI/AISC 360-16. 2016. "*Specification for structural steel buildings*." American Institute of Steel Construction (AISC), Chicago, Illinois.

[4] ATC-24. 1992. "*Guidelines for cyclic seismic testing of components of steel structures*." Applied Technology Council, Redwood City, CA.

[5] Birtel, V., and P. Mark. 2006. "Parameterised finite element modelling of RC beam shear failure." In *Proc., 19th Annual Int. ABAQUS Users' Conf.*, 95-108. Providence, RI: ABAQUS, Inc.

[6] CEN (European Committee for Standardization). 2004. "*Design of composite steel and concrete structures-Part 1-1: General rules and rules for buildings*." EN 1994-1-1: Eurocode 4. Brussels, Belgium: CEN.

[7] Chen, B., Y. Zou, C. Tang, X. Yang, and M. He. 2014. "Contrast research on square and circular CFST laced columns pseudo-static test." *Chin. Civil Eng. J.* 47(Suppl. 2): 108-112. https://doi.org/10.15951/j.tmgcxb.2014.s2.017.

[8] DBJ/T13-51. 2010. "*Technical specification for concrete-filled steel tubular structures*." Housing

and Urban Construction Department of Fujian Province. Fujian, China.

[9] Deng, X. 2012. "*Study on the seismic performance of concrete filled steel tubular lattice column*." Master dissertation, Central South University, Changsha, China.

[10] Fukumoto, T., and K. Morita. 2023. "Restoring force characteristic model for bending moment–rotation angle relationship of concrete-filled square steel tube beam-columns." *Jpn. Archit. Rev.* 6(1): e12351. https://doi.org/10.1002/2475-8876.12351.

[11] GB 50017. 2017. "*Standard for design of steel structures*." Beijing: China Architecture & Building Press.

[12] GB 50936. 2014. "*Technical code for concrete filled steel tubular structures*." Beijing: China Architecture & Building Press.

[13] Goto, Y., G. P. Kumar, and N. Kawanishi. 2010. "Nonlinear finite-element analysis for hysteretic behavior of thin-walled circular steel columns with in-filled concrete." *J. Struct. Eng.* 136(11): 1413-1422. https://doi.org/10.1061/(ASCE) ST.1943-541X.0000240.

[14] Han, L. H., F. Y. Liao, Z. Tao, and Z. Hong. 2009. "Performance of concrete filled steel tube reinforced concrete columns subjected to cyclic bending." *J. Constr. Steel Res.* 65(8–9): 1607-1616. https://doi.org/10.1016/j.jcsr.2009.03.013.

[15] Han, L. H., W. Li, and R. Bjorhovde. 2014. "Developments and advanced applications of concrete-filled steel tubular (CFST) structures: members." *J. Constr. Steel Res.* 100: 211-228. https://doi.org/10.1016/j.jcsr.2014.04.016.

[16] Han, L. H., Y. F. Yang, H. Yang, and W. Li. 2020. "Life-cycle based analytical theory of concrete-filled steel tubular structures and its applications." *Chin. Sci. Bull.* 65(28-29): 3173-3184. https://doi.org/10.1360/TB-2020-0618.

[17] Han, L. H., G. H. Yao, and Z. Tao. 2007. "Performance of concrete-filled thin-walled steel tubes under pure torsion." *Thin-Walled Struct.* 45(1): 24-36. https://doi.org/10.1016/j.tws.2007.01.008.

[18] Huang, Y. 2015. “*Seismic behavior of concrete filled steel tubular built-up columns*.” Ph.D. dissertation, University of Trento, Trento, Italy.

[19] Huang, Z., L. Z. Jiang, Y. F. Chen, Y. Lu, and W. B. Zhou. 2018. “Experimental study on the seismic performance of concrete filled steel tubular laced columns.” *Steel Compos. Struct.* 26(6): 719-731. https://doi.org/10.12989/scs.2018.26.6.719.

[20] JGJ/T 101. 2015. “*Specification for seismic test of buildings*.” Beijing: China Architecture & Building Press.

[21] Ji, X., H. Kang, X. Chen, and J. Qian. 2014. “Seismic behavior and strength capacity of steel tube-reinforced concrete composite columns.” *Earthquake Eng. Struct. Dyn.* 43(4): 487-505. https://doi.org/10.1002/eqe.2354.

[22] Jia, L. J., and H. Kuwamura. 2014. “Prediction of cyclic behaviors of mild steel at large plastic strain using coupon test results.” *J. Struct. Eng.* 140(2): 04013056. https://doi.org/10.1061/(ASCE)ST.1943-541X.0000848.

[23] Kawano, A., and K. Sakino. 2003. “Seismic resistance of CFT trusses.” *Eng. Struct.* 25(5): 607-619. https://doi.org/10.1016/S0141-0296(02)00170-0.

[24] Kawano, A., C. Matsui, and Y. Sakino. 1996. “An experimental study on the elasto-plastic behavior and deformability of concrete-filled tubular truss beam-columns under cyclic loading.” *J. Struct. Constr. Eng.* 61(482): 141-150. https://doi.org/10.3130/aijs.61.141_2.

[25] Lai, Z., A. H. Varma, and L. G. Griffis. 2016. “Analysis and design of noncompact and slender CFT beam-columns.” *J. Struct. Eng.* 142(1): 04015097. https://doi.org/10.1061/(ASCE)ST.1943-541X.0001349.

[26] Lin, S., Y. G. Zhao, Z. H. Lu, and X. F. Yan. 2021. “Unified theoretical model for axially loaded concrete-filled steel tube stub columns with different cross-sectional shapes.” *J. Struct. Eng.* 147(10): 04021159. https://doi.org/10.1061/(ASCE)ST.1943-541X.0003150.

[27] Liu, M., F. Wu, E. Abi, L. Wu, and G. Su. 2022. “Strength degradation characteristics of the steel-concrete interface under cyclic shear.” *Teh. Vjesn.* 29(4): 1372-1381. https://doi.org/10.17559/TV-20210705101118.

[28] Luo, Y. 2013. “*Studies on the seismic performance of four-tube concrete filled steel tubular laced columns*.” Master dissertation, Central South University, Changsha, China.

[29] Ma, D. Y., L. H. Han, W. Li, and X. L. Zhao. 2018. “Seismic performance of concrete-encased CFST piers: Analysis.” *J. Bridge Eng.* 23(1): 04017119. https://10.1061/(ASCE)BE.1943-5592.0001157.

[30] Matsui, C., and A. Kawano. 1988. “Strnegth and behavior of concrete-filled tubular truss.” *In: Proceedings of the International Speciality Conference on Concrete Filled Steel Tubular Structures*, 113-119. Harbin, China.

[31] Shi, Y., M. Wang, and Y. Wang. 2011. “Experimental and constitutive model study of structural steel under cyclic loading.” *J. Constr. Steel Res.* 67(8): 1185-1197. https://doi.org/10.1016/j.jcsr.2011.02.011.

[32] Varma, A. H., J. M. Ricles, R. Sause, and L. W. Lu. 2004. “Seismic behavior and design of high-strength square concrete-filled steel tube beam columns.” *J. Struct. Eng.* 130(2): 169-179. https://doi.org/10.1061/(ASCE)0733-9445(2004)130:2(169).

[33] Yang, Y. F., C. Hou, and M. Liu. 2018a. “Experimental study and numerical analysis of CFSST columns subjected to lateral cyclic loading.” *J. Struct. Eng.* 144(12): 04018219. https://doi.org/10.1061/(ASCE)ST.1943-541X.0002225.

[34] Yang, Y. F., M. Liu, and F. Fu. 2018b. “Experimental and numerical investigation on the performance of three-legged CFST latticed columns under lateral cyclic loadings.” *Thin-Walled Struct.* 132: 176-194. https://doi.org/10.1016/j.tws.2018.08.016.

[35] Yang, Y. F., M. Liu, C. Hou, and X. M. Bie. 2019. “Behaviour of four-legged square CFST

latticed members under lateral cyclic loading." *J. Constr. Steel Res.* 156: 54-74. https://doi.org/10.1016/j.jcsr.2019.01.018.

[36] Yang, Y. F., M. Liu, and X. M. Bie. 2022. "A research on the bearing capacity of four-legged CFST latticed members under axial compression." *Prog. Steel Build. Struct.* 24(5): 18-26. https://doi.org/10.13969/j.cnki.cn31-1893.2022.05.003.

[37] Yuan, H., Q. Wu, Y. Huang, and Z. She. 2020. "Experimental and theoretical studies on the seismic performance of CFST battened built-up column piers." *Eng. Struct.* 206: 110099. https://doi.org/10.1016/j.engstruct.2019.110099.

Table Caption List

Table 1. Summary of available cyclic tests on the CFST latticed beam-columns.

Table 2. Information of the specimens.

Table 3. Material properties of steel CHS.

Table 4. Parameters in the mixed hardening plasticity model of steel tube.

Table 5. Parameters for ductile damage initiation criterion of steel tube.

Tables:

Table 1. Summary of available cyclic tests on the CFST latticed beam-columns.

No.	Section form	Layout of lacings	L (mm)	$D\times T$ (mm×mm)	$d\times t$ (mm×mm)	$f_{y,li}$ (MPa)	f_c' (MPa)	n	Number of specimens	Ref.
1	Two-limbed	V-shape	2434	○-60.5×2.3	○-34×2.0	370.4	29.4	0-0.2	8	Kawano et al. (1996)
2	Three-limbed	M-shape	1960	○-100× 1.9/4.0	○-34×2.5	303.4/ 325.2	45.9	0.05~ 0.52	6	Yang et al. (2018b)
3	Four-limbed	M-shape	1200	○-86×1.5	○-48×2.5	315.0	34.2~ 50.0	0.2~0.4	8	Deng (2012)
4	Four-limbed	N-shape	1700	○-90×3.4	○-42×2.7	259.0	57.9	0.2	1	Chen et al. (2014)
				□-80×3.0					2	
5	Four-limbed	| |-, V-, M- and N-shape	2500	○-110×2.0	○-50×2.0	345.0	32.1~ 47.5	0.15	6	Huang (2015)
6	Four-limbed	M-shape	1200~ 3000	○-86×1.5	○-48×2.0 ~3.0	315.0	16.3	0.2~ 0.3	4	Huang et al. (2018)
7	Four-limbed	M-shape	1960	□-100× 1.8/3.5	□-34×2.5	297.6/ 275.5	59.3	0.05~ 0.5	6	Yang et al. (2019)
8	Four-limbed	| |-shape	2500	○-114×2.0	○-48×2.0	345.0	34.1~ 54.6	0.15	7	Yuan et al. (2020)

Note: The limb tubes/lacings of each specimen have the same section size and physical properties, and '○' and '□' denote circular hollow section (CHS) and square hollow section (SHS), respectively.

Table 2. Information of the specimens.

No.	Label	$D\times T$ (mm)	$d\times t$ (mm)	λ_e	D/T	n	N_0 (kN)	$P_{u,e}$ (kN)	$K_{a,e}$ (kN/mm)	I_d
1	S-A-0.25	○-100×1.94	○-34×2.46	27.7	51.5	0.25	182.5	66.0	3.38	2.56
2	S-B-0.25	○-100×4.01	○-34×2.46	31.1	24.9	0.25	344.1	140.5	4.72	3.47
3	C-A-0.05	○-100×1.94	○-34×2.46	35.1	51.5	0.05	93.7	117.9	8.45	5.78
4	C-A-0.25	○-100×1.94	○-34×2.46	35.1	51.5	0.25	468.5	128.7	7.46	4.35
5	C-A-0.50	○-100×1.94	○-34×2.46	35.1	51.5	0.50	937.0	131.2	7.13	4.13
6	C-B-0.05	○-100×4.01	○-34×2.46	36.8	24.9	0.05	131.0	181.2	11.00	6.42
7	C-B-0.25	○-100×4.01	○-34×2.46	36.8	24.9	0.25	654.9	172.2	10.54	4.68
8	C-B-0.50	○-100×4.01	○-34×2.46	36.8	24.9	0.50	1309.9	154.8	10.20	4.45

Note: 1) 'S' and 'C' represent steel CHS limb and circular CFST limb, respectively; 2) 'A' and 'B' represent D/T value of steel CHS in the limbs of 51.5 and 24.9, respectively; and 3) the values of 0.05, 0.25 and 0.50 indicate the axial compression level.

Table 3. Material properties of steel CHS.

Type	Diameter (mm)	Thickness (mm)	Yield strength (MPa)	Tensile strength (MPa)	Elastic modulus (N/mm^2)	Poisson's ratio	Elongation (%)
Limb	100	1.94	325.2	413.2	1.80×10^5	0.289	19.9
	100	4.01	303.4	426.2	1.96×10^5	0.274	20.1
Lacing	34	2.46	332.4	452.3	2.00×10^5	0.300	-

Table 4. Parameters in the mixed hardening plasticity model of steel tube.

Type	$D\times T/d\times t$ (mm×mm)	Isotropic hardening			Nonlinear kinematic hardening								Ref.
		$\sigma\|_0$ (MPa)	Q_∞ (MPa)	b_s	$C_{kin,1}$ (MPa)	γ_1	$C_{kin,2}$ (MPa)	γ_2	$C_{kin,3}$ (MPa)	γ_3	$C_{kin,4}$ (MPa)	γ_4	
Limb	60.5×2.3	370.4	21	1.2	8450.2	175.5	7176.9	115.1	2814.3	34.5	1556.2	27.6	Kawano et al. (1996)
Lacing	34×2.0	381.2			8644.6	175.7	7348.6	114.7	2797.4	34.7	1601.4	27.0	
Limb	86×1.5	315.0	21	1.2	7453.0	174.5	6296.0	117.1	2900.9	33.5	1324.5	30.6	Deng (2012)
Lacing	48×2.5												
Limb	110×2.0	345.0	21	1.2	7993.0	175.0	6773.0	116.0	2854.0	34.0	1450.0	29.0	Huang (2015)
Lacing	50×2.0	374.0			8515.0	175.5	7234.1	114.9	2808.7	34.5	1571.3	27.4	
Limb	86×1.5	315.0	21	1.2	7453.0	174.5	6296.0	117.1	2900.9	33.5	1324.5	30.6	Huang et al. (2018)
Lacing	48×2.0/3.0	320.0			7543.0	174.5	6375.5	116.9	2893.1	33.5	1345.5	30.4	
Limb	100×1.94	325.2	21	1.2	7636.6	174.6	6458.2	116.7	2885.0	33.6	1367.2	30.1	This paper
	100×4.01	303.4			7244.2	174.2	6111.6	117.5	2919.0	33.2	1276.0	31.3	
Lacing	34×2.46	332.4			7766.2	174.8	6572.7	116.5	2873.7	33.8	1397.3	29.7	

Table 5. Parameters for ductile damage initiation criterion of steel tube.

Type	$D\times T/d\times t$ (mm×mm)	K_p (MPa)	m_s	C_1	C_2
Limb	100×1.94	582.76	0.103	0.055	0.222
	100×4.01	652.25	0.145	0.083	0.224
Lacing	34×2.46	680.97	0.135	0.077	0.223

Figures:

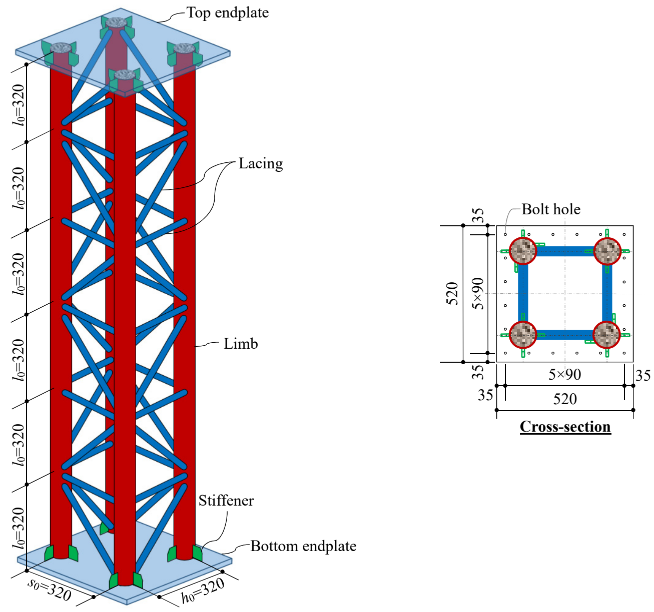

Fig. 1. Configuration and dimensions of the specimens (units are in millimeters).

Fig 2

Click here to access/download;Figure;Fig. 02.pdf

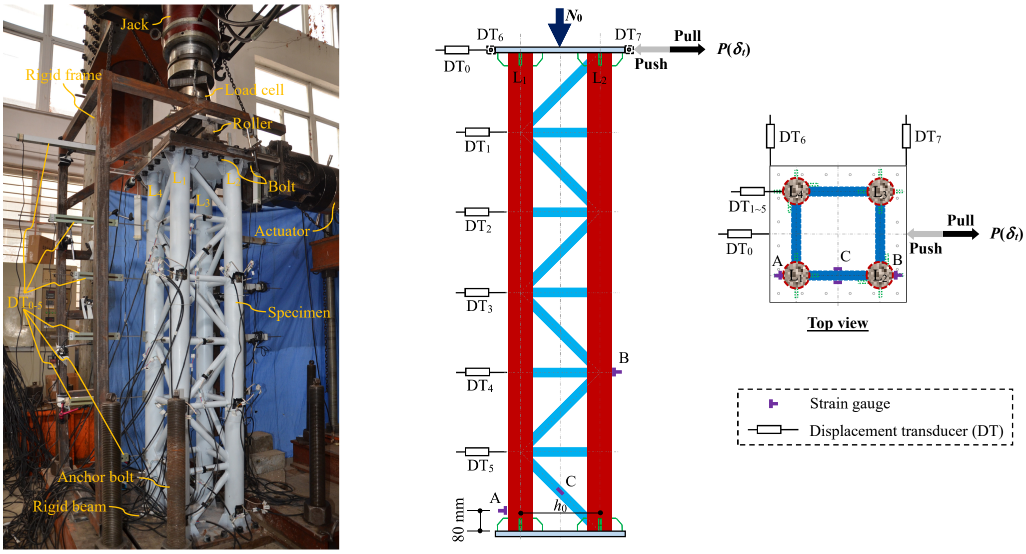

Fig. 2. Testing set-up and instrumentation.

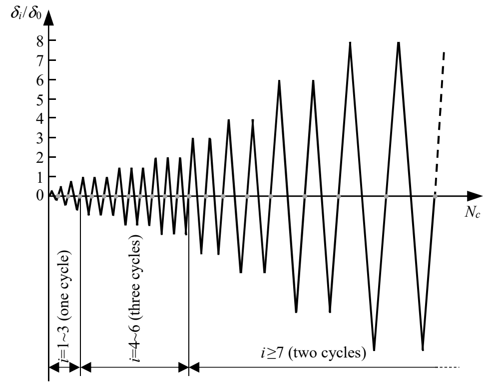

Fig. 3. History of lateral displacement.

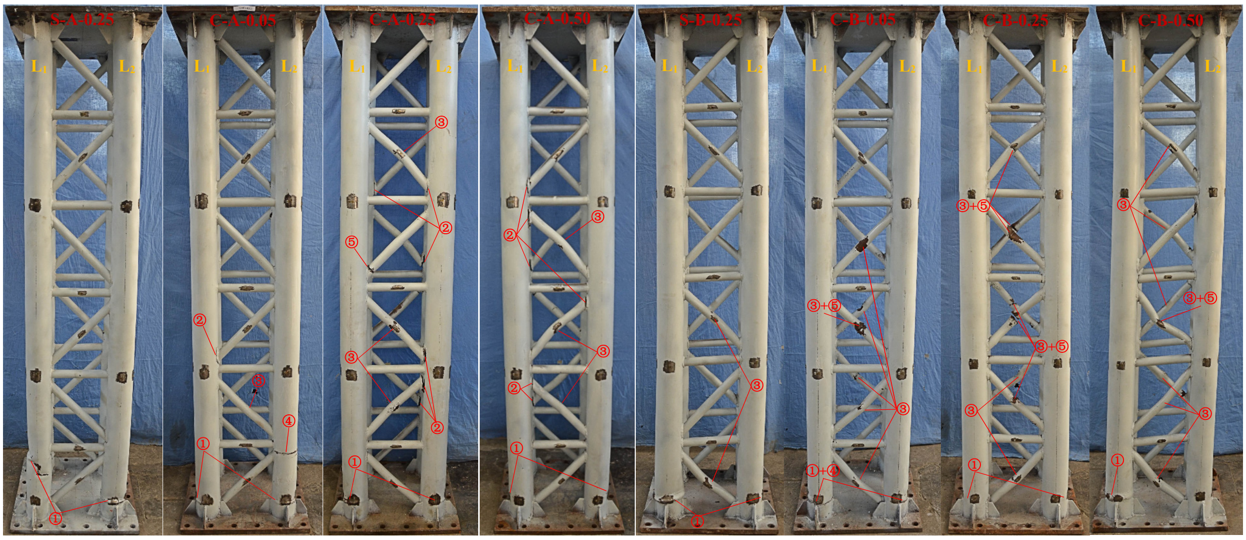

(a)

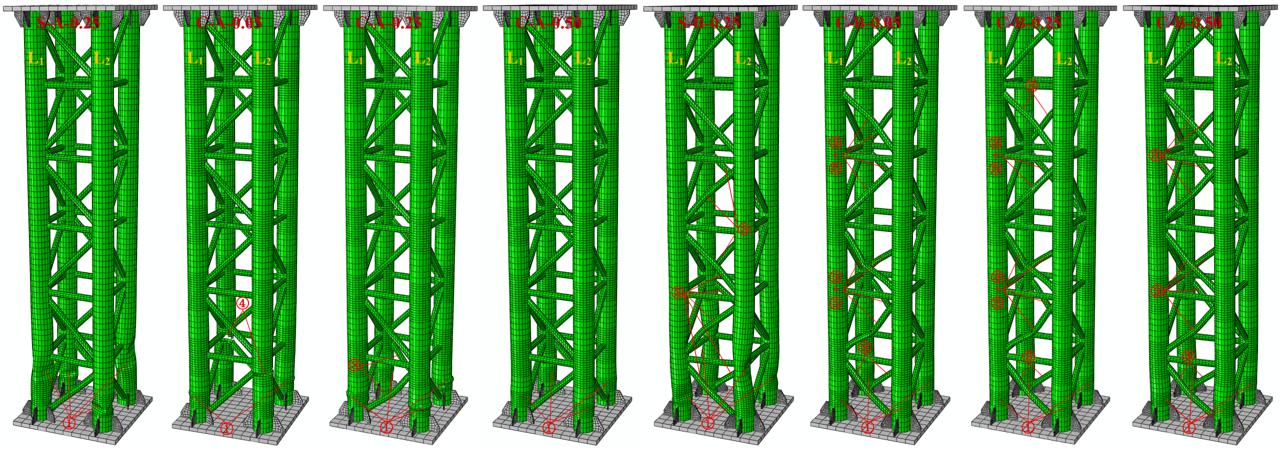

(b)

Fig. 4. Failure modes of the specimens: (a) tested result; and (b) predicted result.

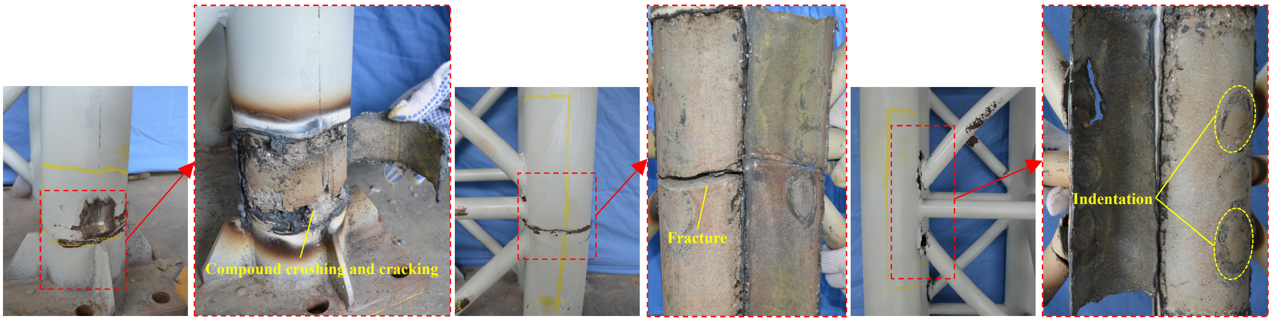

(a) (b) (c)

Fig. 5. Representative failure modes of concrete core in the CFST limbs: (a) compound crushing and cracking; (b) fracture; and (c) indentation.

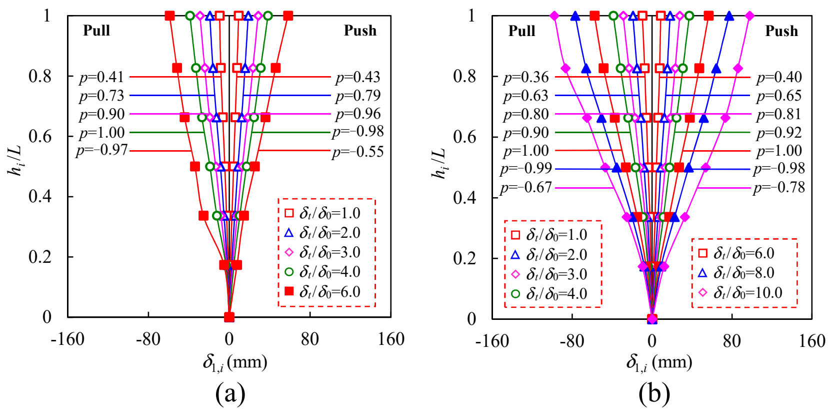

Fig. 6. Lateral displacement along the length of typical specimens: (a) S-A-0.25; and (b) C-A-0.25.

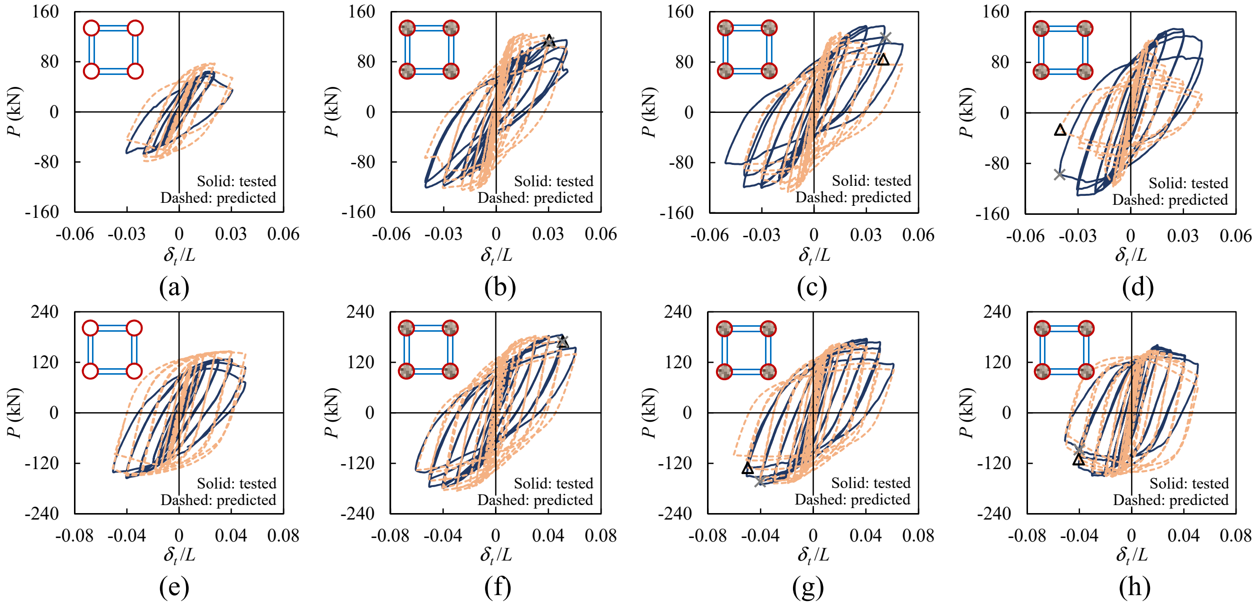

Fig. 7. $P - \delta_t/L$ hysteretic curve of the specimens: (a) S-A-0.25; (b) C-A-0.05; (c) C-A-0.25; (d) C-A-0.50; (e) S-B-0.25; (f) C-B-0.05; (g) C-B-0.25; and (h) C-B-0.50.
(×: tested starting point of limb tube cracking; and Δ: predicted starting point of limb tube cracking)

Fig 8 Click here to access/download;Figure;Fig. 08.pdf

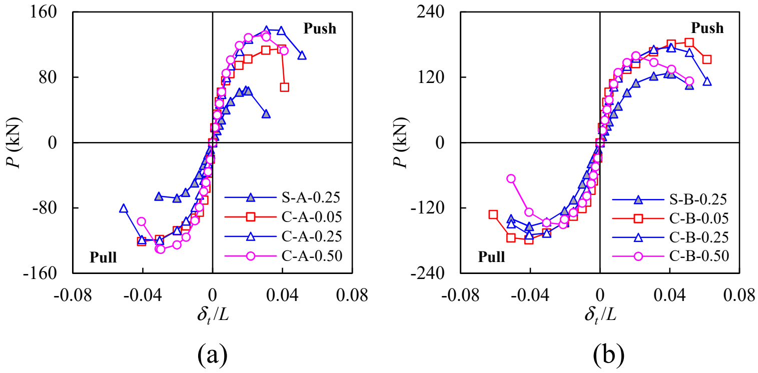

Fig. 8. Effect of parameters on $P-\delta_t/L$ backbone curve of the specimens: (a) *D*/*T*=51.5; and (b) *D*/*T*=24.9.

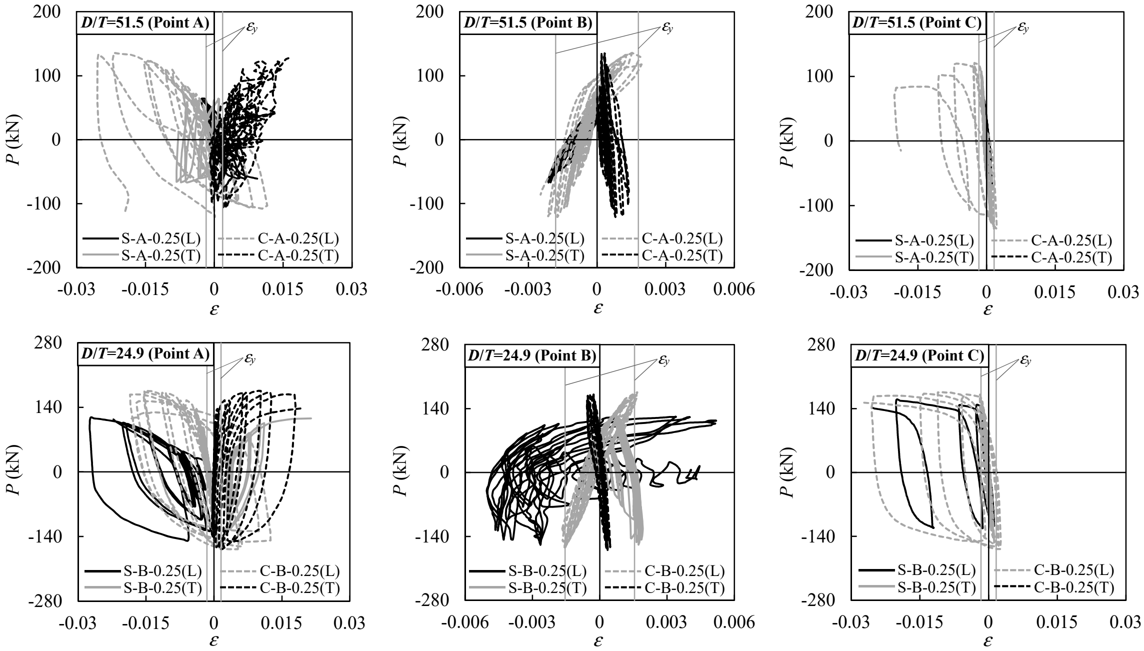

(a)

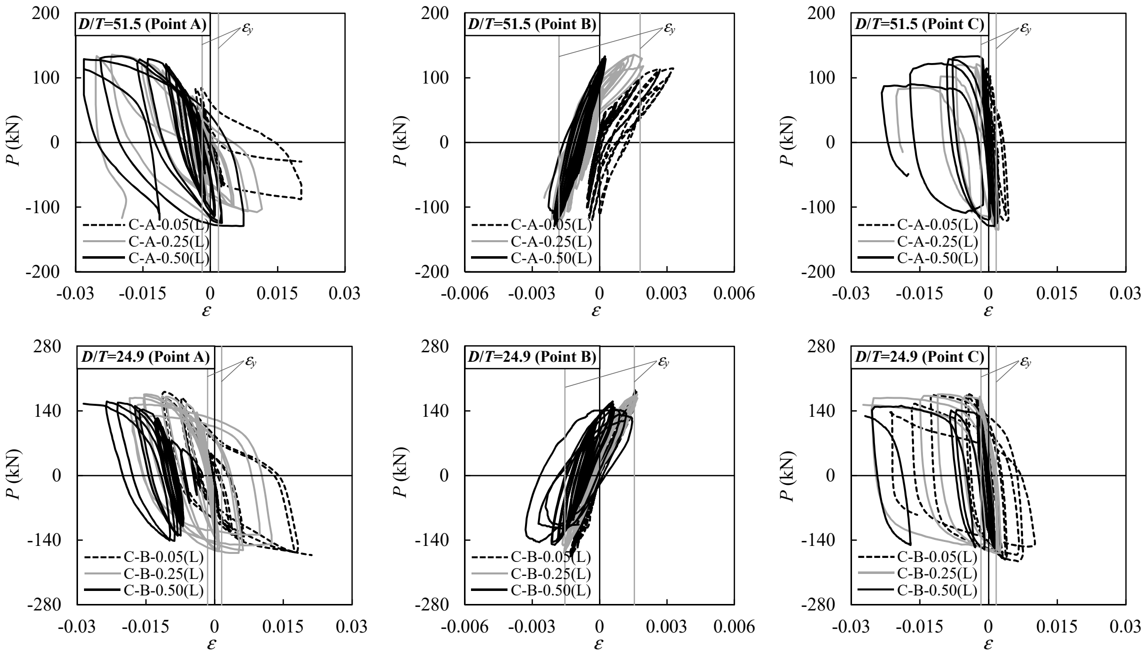

(b)

Fig. 9. Effect of parameters on $P-\varepsilon$ hysteretic curves: (a) type of limb; and (b) axial compression level.

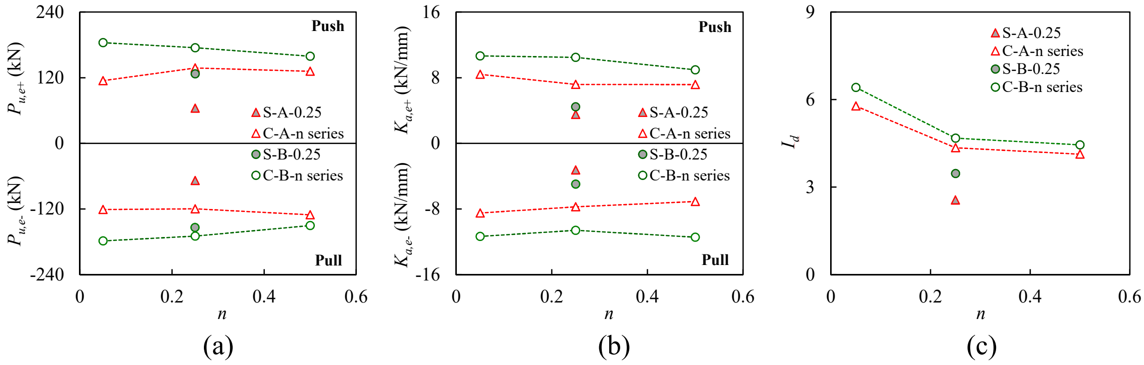

Fig. 10. Variation in mechanical factors of the specimens: (a) lateral capacity; (b) elastic stiffness; and (c) ductility index.

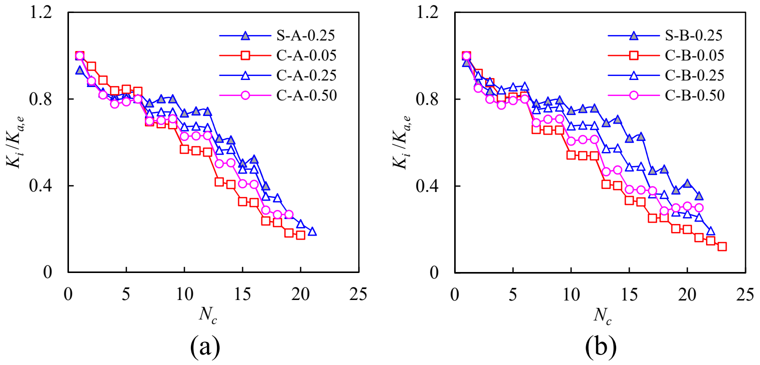

Fig. 11. Deterioration of stiffness of the specimens: (a) D/T=51.5; and (b) D/T=24.9.

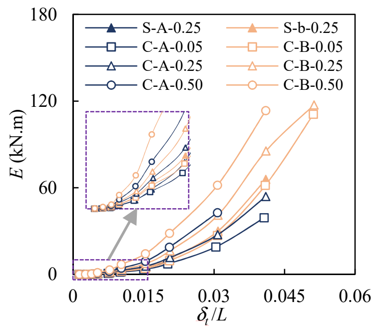

Fig. 12. Effect of parameters on $E - \delta_t/L$ relationship.

Fig 13 Click here to access/download;Figure;Fig. 13.pdf

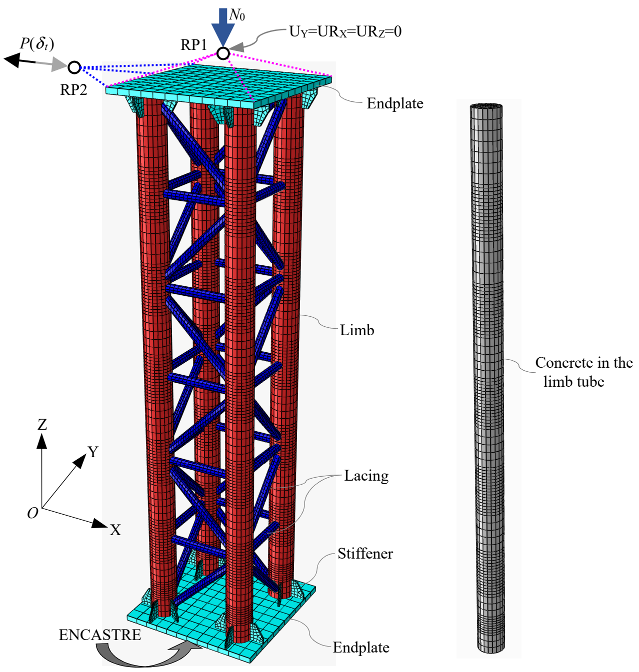

Fig. 13. Meshing and boundary conditions of the FE model.

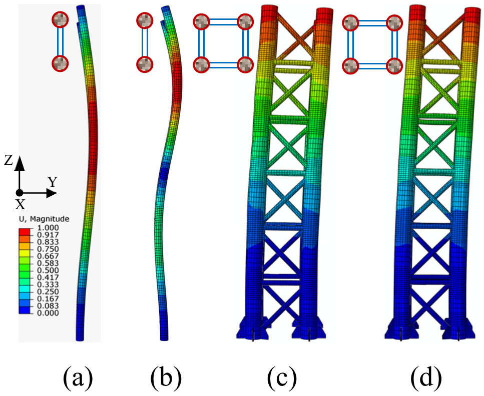

Fig. 14. First buckling eigenmode of limb tubes and lacings in typical composite specimens (Ampification factor=100): (a) CN1R; (b) CB1R; (c) C-A-n; and (d) C-B-n.

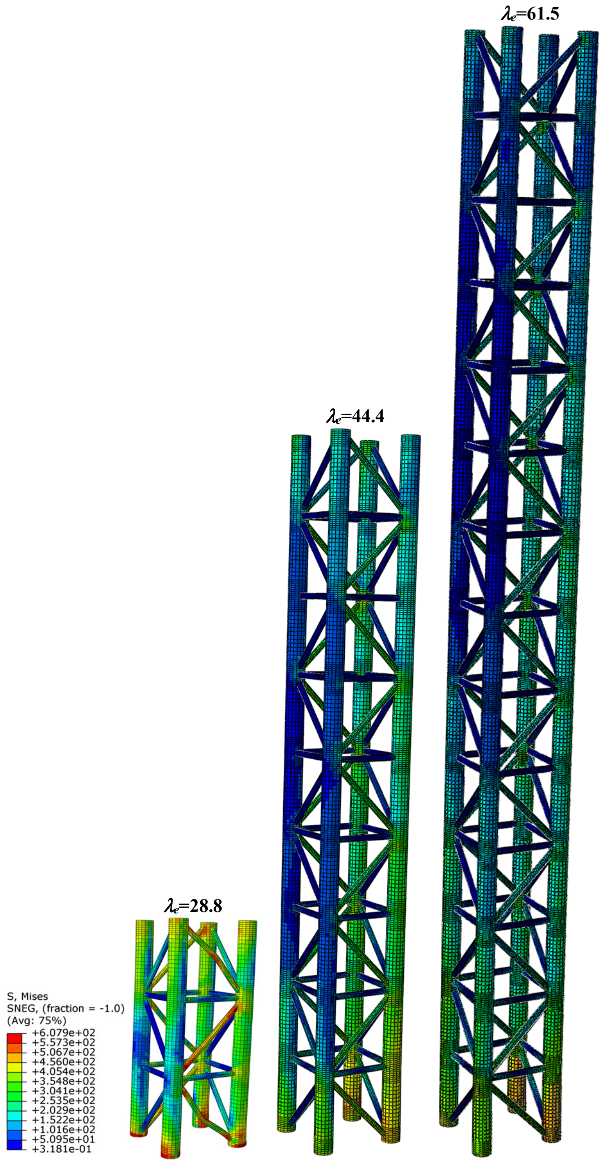

Fig. 15. Effect of λ_e on the failure modes of typical four-limbed circular CFST latticed beam-columns.

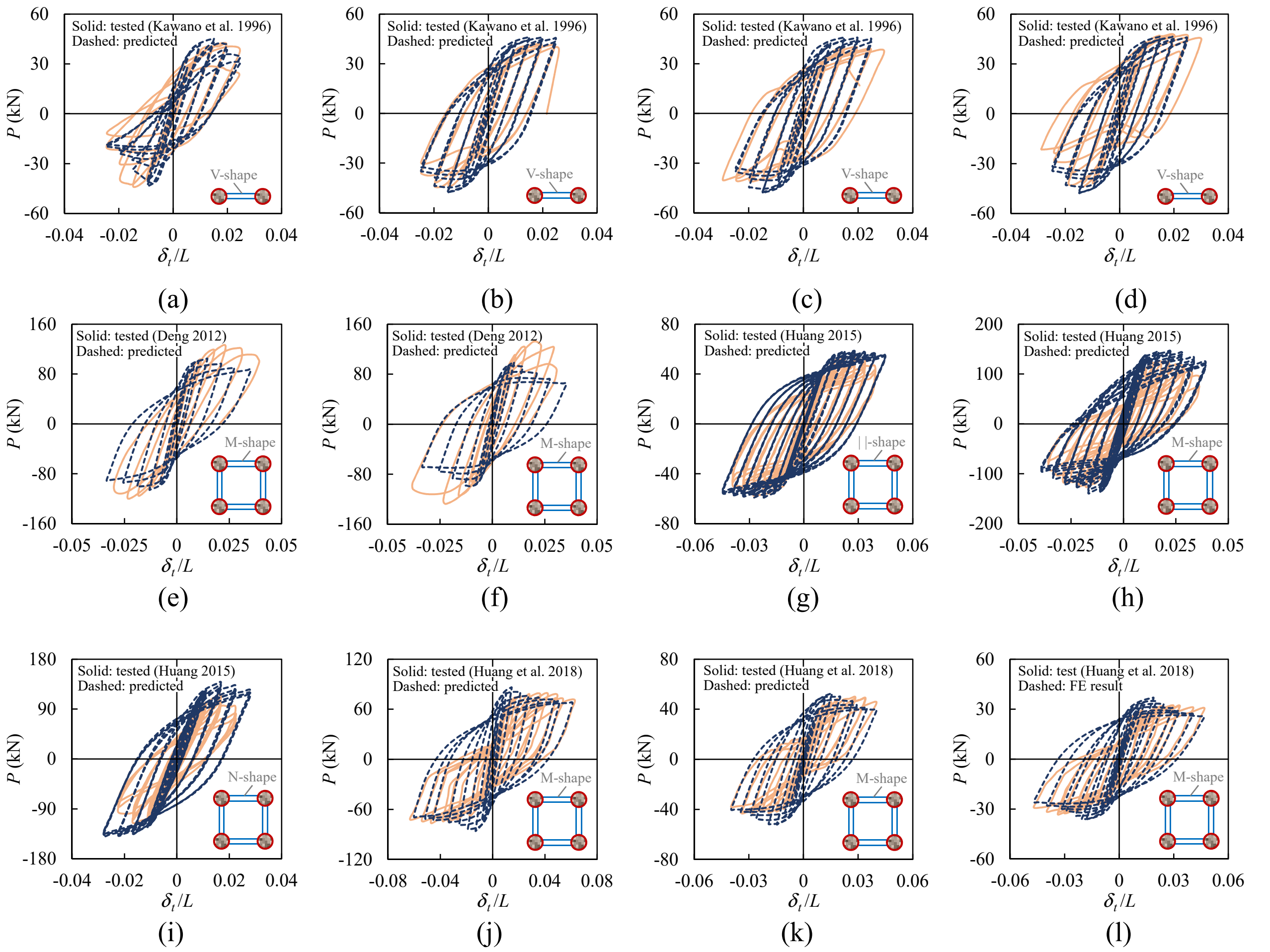

Fig. 16. Typical comparison between the predicted $P - \delta_t/L$ hysteretic curves and the tested results in the literature: (a) CN1R; (b) CB1R; (c) CB0R; (d) CB2R; (e) GZZ1; (f) GZZ3; (g) S1; (h) S5; (i) S6; (j) SCC1; (k) SCC5; and (l) SCC6.

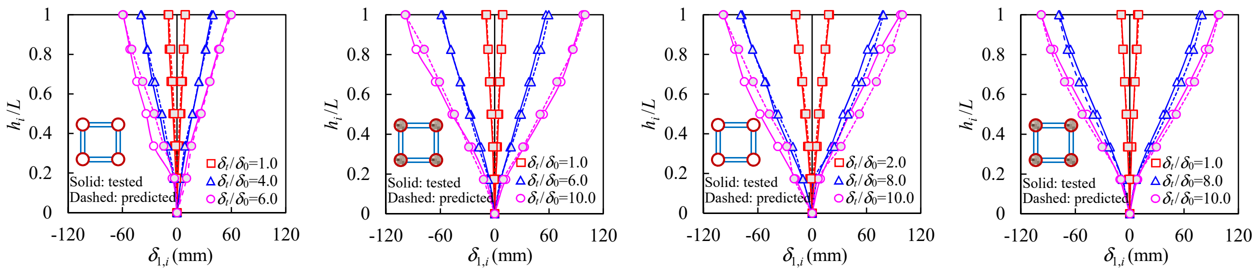

(a) (b) (c) (d)

Fig. 17. Typical comparison between the predicted and tested lateral displacement distribution of the specimens: (a) S-A-0.25; (b) C-A-0.25; (c) S-B-0.25; and (d) C-B-0.25.

Fig 18 Click here to access/download;Figure;Fig. 18.pdf

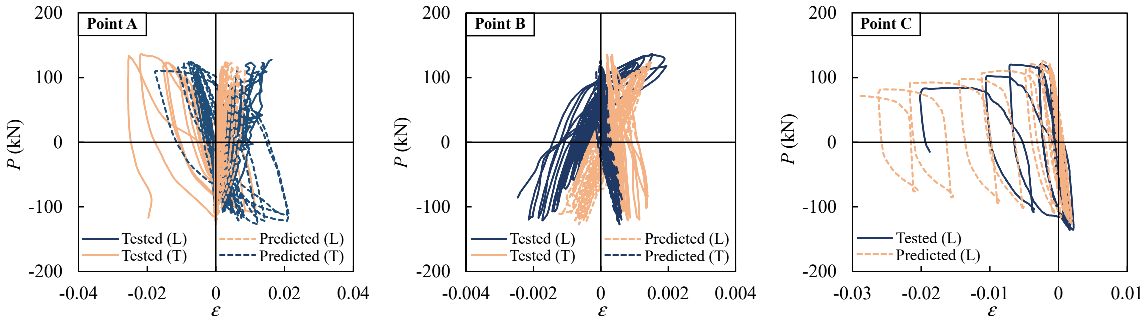

(a)

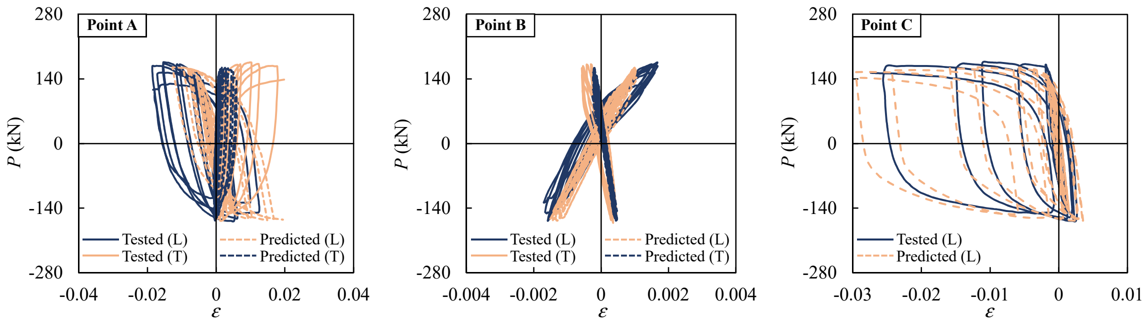

(b)

Fig. 18. Comparison between the predicted and tested P–ε hysteretic curves of typical specimens: (a) C-A-0.25; and (b) C-B-0.25.

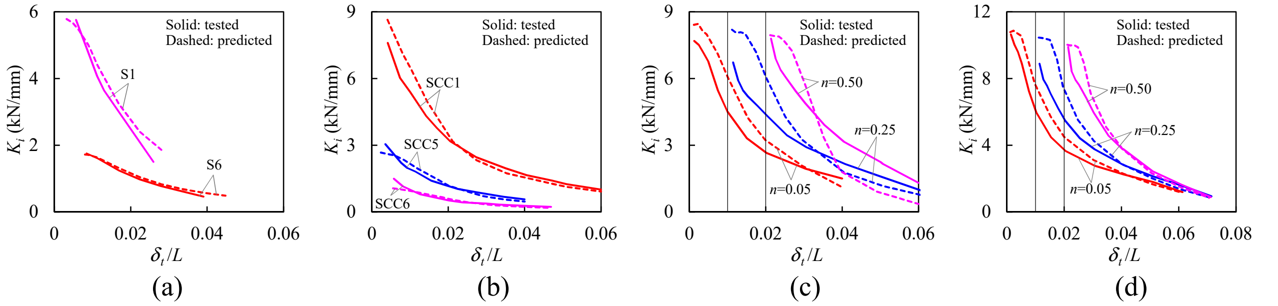

Fig. 19. Comparison between the predicted and tested deterioration of stiffness: (a) specimens in Huang (2015); (b) specimens in Huang et al. (2018); (c) specimens (C-A-n series) in this study; and (d) specimens (C-B-n series) in this study.

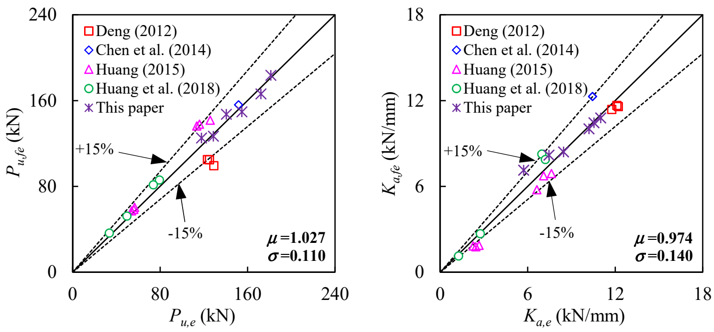

(a) (b)

Fig. 20. Comparison between the predicted and tested mechanical factors: (a) lateral capacity; and (b) elastic stiffness.

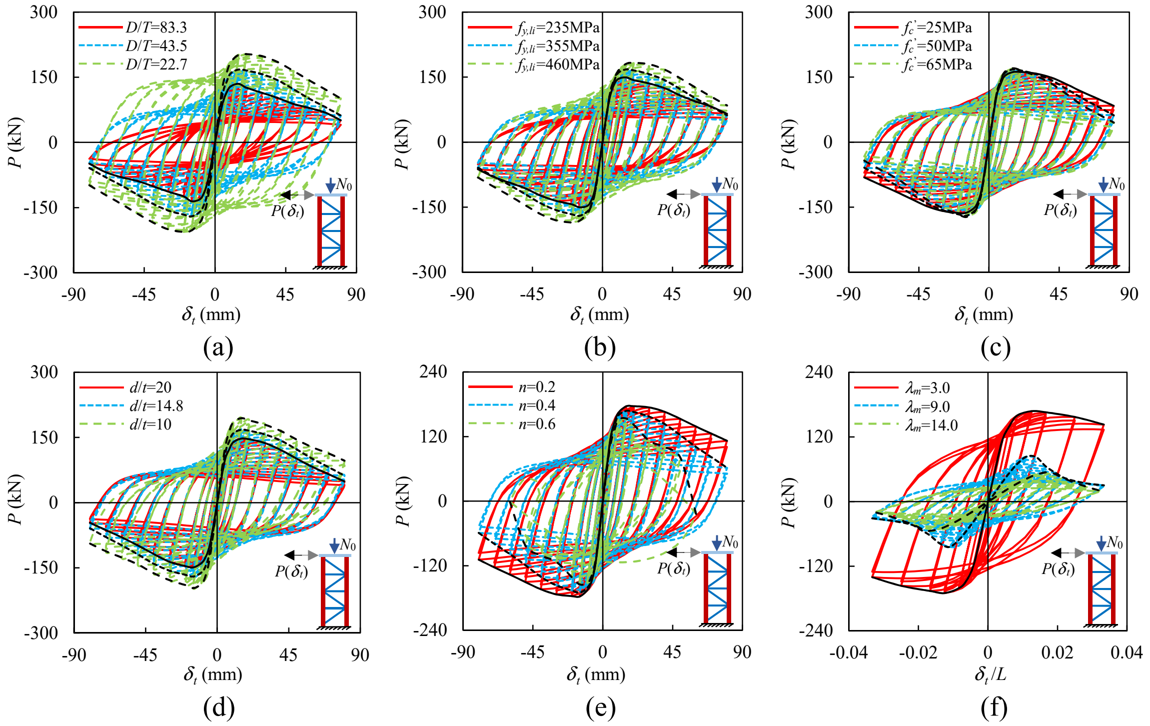

Fig. 21. Effect of main parameters on $P-\delta_t$ hysteretic curve of four-limbed circular CFST latticed beam-columns: (a) D/T; (b) $f_{y,li}$; (c) f_c'; (d) d/t; (e) n; and (f) λ_m.

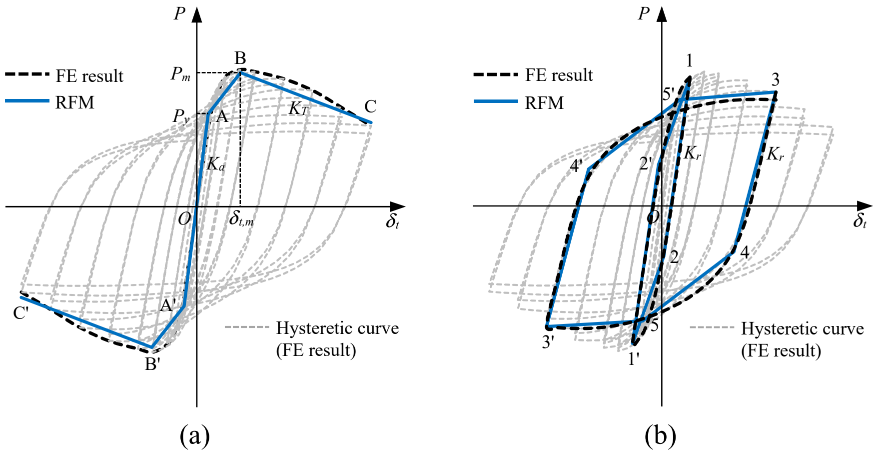

Fig. 22. RFM of four-limbed circular CFST latticed beam-columns: (a) backbone curve; and (b) unloading/reloading paths.

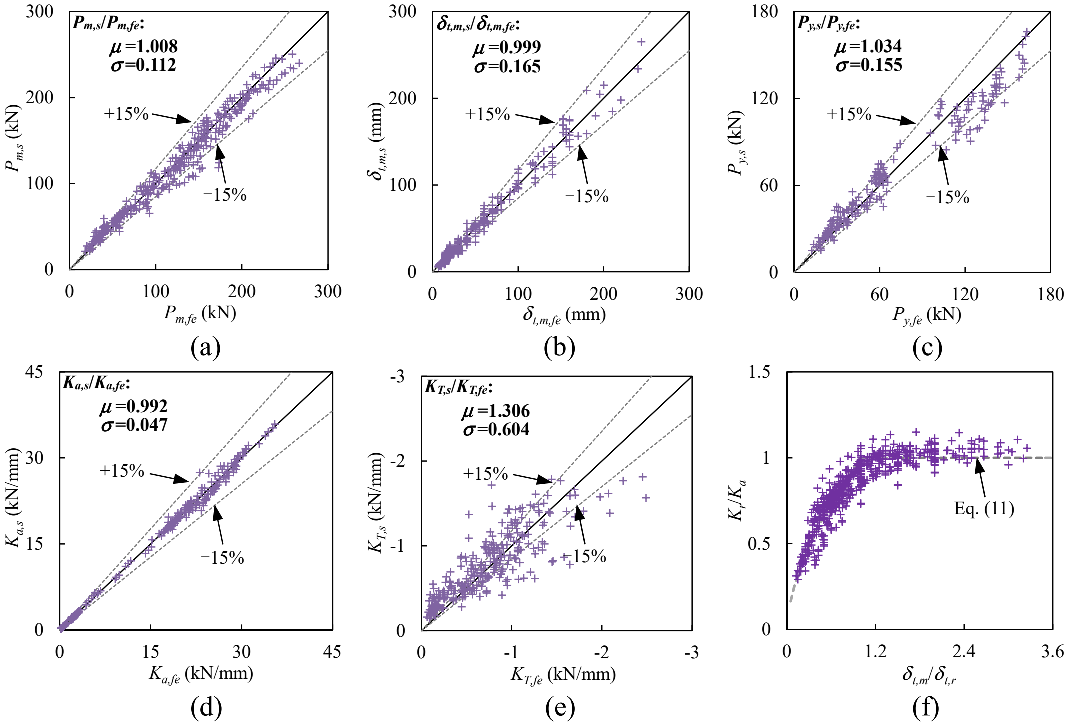

Fig. 23. Comparison of key parameters in the RFM between the simplified and FE simulation results: (a) P_m; (b) $\delta_{t,m}$; (c) P_y; (d) K_a; (e) K_T; and (f) K_r/K_a-$\delta_{t,m}/\delta_{t,r}$ relationship.

Fig 24

Click here to access/download;Figure;Fig. 24.pdf

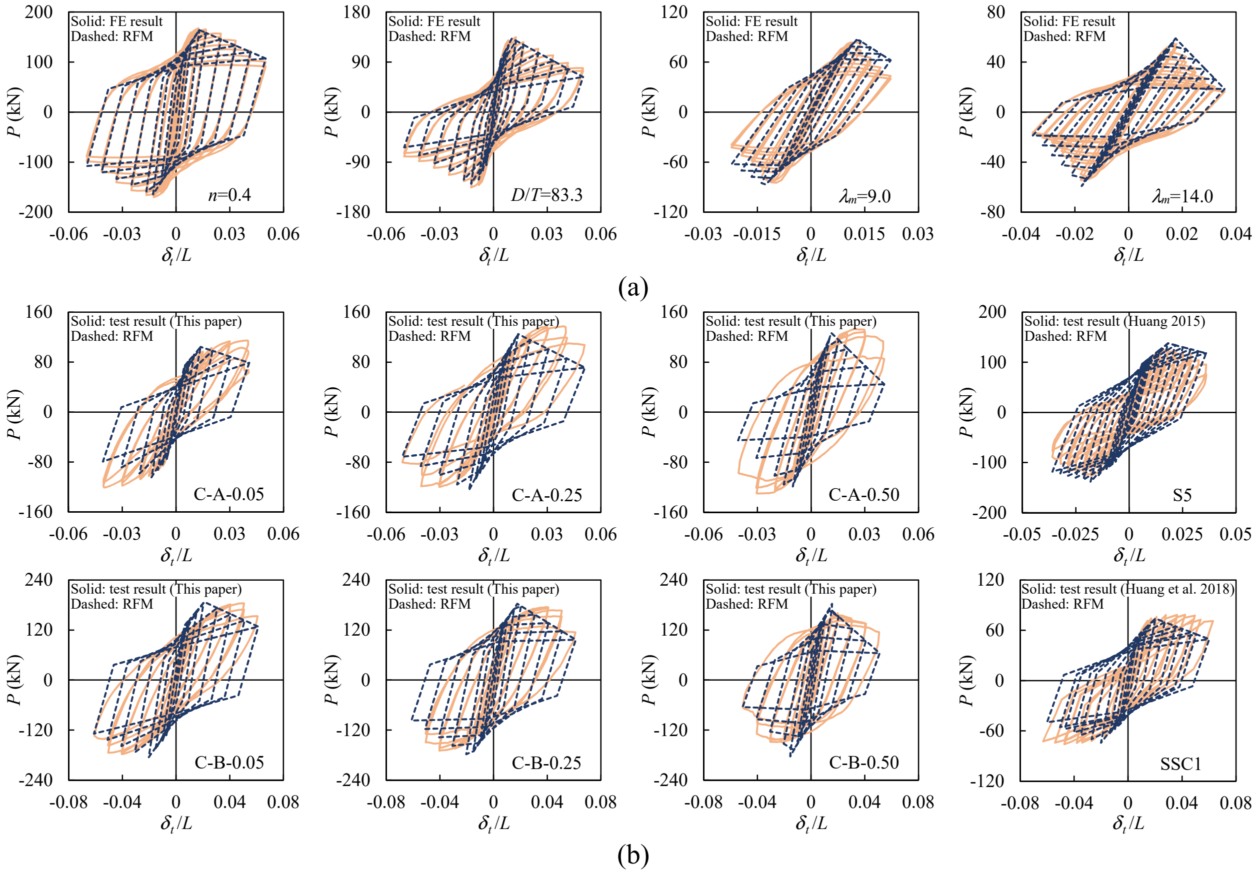

Fig. 24. Typical comparison between the RFM and FE/test $P-\delta_t/L$ hysteretic curves: (a) RFM and FE result; and (b) RFM and test result.

Fig. 1. Configuration and dimensions of the specimens (units are in millimeters).

Fig. 2. Testing set-up and instrumentation.

Fig. 3. History of lateral displacement.

Fig. 4. Failure modes of the specimens: (a) tested result; and (b) predicted result.

Fig. 5. Representative failure modes of concrete core in the CFST limbs: (a) compound crushing and cracking; (b) fracture; and (c) indentation.

Fig. 6. Lateral displacement along the length of typical specimens: (a) S-A-0.25; and (b) C-A-0.25.

Fig. 7. $P-\delta_t/L$ hysteretic curve of the specimens: (a) S-A-0.25; (b) C-A-0.05; (c) C-A-0.25; (d) C-A-0.50; (e) S-B-0.25; (f) C-B-0.05; (g) C-B-0.25; and (h) C-B-0.50.

Fig. 8. Effect of parameters on $P-\delta_t/L$ backbone curve of the specimens: (a) D/T=51.5; and (b) D/T=24.9.

Fig. 9. Effect of parameters on $P-\varepsilon$ hysteretic curves: (a) type of limb; and (b) axial compression level.

Fig. 10. Variation in mechanical factors of the specimens: (a) lateral capacity; (b) elastic stiffness; and (c) ductility index.

Fig. 11. Deterioration of stiffness of the specimens: (a) D/T=51.5; and (b) D/T=24.9.

Fig. 12. Effect of parameters on $E-\delta_t/L$ relationship.

Fig. 13. Meshing and boundary conditions of the FE model.

Fig. 14. First buckling eigenmode of limb tubes and lacings in typical composite specimens (Ampification factor=100): (a) CN1R; (b) CB1R; (c) C-A-n; and (d) C-B-n.

Fig. 15. Effect of λ_e on the failure modes of typical four-limbed circular CFST latticed beam-columns.

Fig. 16. Typical comparison between the predicted $P-\delta_t/L$ hysteretic curves and the tested results in the literature: (a) CN1R; (b) CB1R; (c) CB0R; (d) CB2R; (e) GZZ1; (f) GZZ3; (g) S1; (h) S5; (i) S6; (j) SCC1; (k) SCC5; and (l) SCC6.

Fig. 17. Typical comparison between the predicted and tested lateral displacement distribution of the specimens: (a) S-A-0.25; (b) C-A-0.25; (c) S-B-0.25; and (d) C-B-0.25.

Fig. 18. Comparison between the predicted and tested $P-\varepsilon$ hysteretic curves of typical specimens: (a) C-A-0.25; and (b) C-B-0.25.

Fig. 19. Comparison between the predicted and tested deterioration of stiffness: (a) specimens in Huang (2015); (b) specimens in Huang et al. (2018); (c) specimens (C-A-n series) in this study; and (d) specimens (C-B-n series) in this study.

Fig. 20. Comparison between the predicted and tested mechanical factors: (a) lateral capacity; and (b) elastic stiffness.

Fig. 21. Effect of main parameters on $P-\delta_t$ hysteretic curve of four-limbed circular CFST latticed beam-columns: (a) D/T; (b) $f_{y,li}$; (c) f_c'; (d) d/t; (e) n; and (f) λ_m.

Fig. 22. RFM of four-limbed circular CFST latticed beam-columns: (a) backbone curve; and (b) unloading/reloading paths.

Fig. 23. Comparison of key parameters in the RFM between the simplified and FE simulation results: (a) P_m; (b) $\delta_{t,m}$; (c) P_y; (d) K_a; (e) K_T; and (f) K_r/K_a-$\delta_{t,m}/\delta_{t,r}$ relationship.

Fig. 24. Typical comparison between the RFM and FE/test $P-\delta_t/L$ hysteretic curves: (a) RFM and FE result; and (b) RFM and test result.